國 立 交 通 大 學

光 電 工 程 研 究 所

碩 士 論 文

氮化鎵垂直共振腔面射型雷射之電流侷限研究

Study of Current Confinement in GaN-based Vertical-Cavity Surface Emitting Lasers

研究生：陳 政 宏

指導教授：郭 浩 中 教授

盧 廷 昌 教授

中華民國九十九年七月

氮化鎵垂直共振腔面射型雷射之電流局限之研究

Study of current confinement in GaN-based vertical cavity surface emitting lasers

研 究 生：陳政宏　　Student：Cheng-Hung Chen

指導教授：郭浩中　　Advisors：Hao-Chung Kuo

盧廷昌　　Tien-Chang Lu

國 立 交 通 大 學

光 電 工 程 研 究 所

碩 士 論 文

A Thesis
Submitted to Institute of Electro-optical Engineering
College of Electrical Engineering and Computer Science
National Chiao Tung University
in partial Fulfillment of the Requirements
for the Degree of Master
in Electro-Optical Engineering
July 2010
Hsinchu, Taiwan, Republic of China

中 華 民 國 九 十 九 年 七 月

摘要

本篇論文旨在製作電激發氮化鎵垂直型共振腔雷射結構搭配混合式布拉格反射鏡中，透過減薄 ITO 透明導電層的厚度藉此降低光共振在此結構中的內部損耗，以及在量子井上成長氮化鋁做為電流阻擋層取代原來在 p 型氮化鎵上的氮化矽，並且量測其電性及光性作進一步的探討。

首先，我們利用模擬的方式計算出 30nm 的 ITO 透明導電層可以有效的降低內部損耗又可以有效的符合電激發元件所需的電流擴散層效果。此外，本結構也成功製作於電激發氮化鎵垂直型共振腔面射型雷射中。在室溫下，其雷射的臨界操作電流為 9.7mA，起始電壓為 4.3V，具有約 180 歐姆的低電阻。在不同的電流注入下，雷射的頻譜具有單一雷射波長為 412nm，雷射半高寬為 0.5nm。雷射行為也從自激發發光輻射轉變為受激發發光輻射。自激發光耦合因子及雷射發散角分別為 $5*10^{-3}$ 及 8 度左右。

為了更進一步能夠降低閥值電流並將注入電流作有效利用，我們使用了相較於氮化鎵高能隙的氮化鋁(6.2eV)成長在量子井上方，如此的設計可以使電流完全注入量子井內不會因為擴散而造成損失。另外，為了更進一步將共振腔的光學損耗降低，我們設計了環型的透明導電層取代原先的圓型透明導電層，讓共振光不被透明導電層所吸收。 透過量測共振腔中的 Q 值，原先以圓形透明導電層的共振腔 Q 值約為 650 而以環型透明導電之元件 Q 值提升至 1100，與計算結果接近.

在本論文中，我們設計出了室溫電激發面射型雷射並且量測雷射現象，進一步為了提高雷射的效能我們提出將電流做更有效利用的新結構，並且也可提升共振腔的品質因子，這樣的設計對於降低閥值電流於電激發元件上是更有效的方法。

Abstract

We have investigated the electrical and optical performance in GaN-based VCSELs, which take AlN as current blocking layer and conventional type take SiNx as current layer. We have reported the demonstration of the CW laser action on GaN-based vertical cavity surface emitting lasers (VCSEL) at room temperature. The laser has a threshold current of about 9.7 mA corresponding to the current density of about 12.4 kA/cm2 and a turn-on voltage about 4.3 V at 300K. The lasing wavelength was 412 nm with a linewidth of about 0.5 nm. A spontaneous emission coupling efficiency factor of about 5×10-3 and the degree of polarization of about 55% were measured, respectively. The laser beam has a narrow divergence angle of about 8°.

To further decrease the threshold current and optimum the VCSEL structure, we used AlN re-growth on the multiple quantum wells as current blocking layer and optical confined layer. On the other hand, in order to reduce the optical loss in the resonate cavity we take the ring shape ITO to replace the circular ITO layer as usual, through measured the Q factor in the conventional VCSEL the AlN VCSEL, the latter device shows a higher Q factor about 1100 than the conventional 600. It represents that the cavity without ITO layer has a better optical resonate characteristic.

In this report, we demonstrated RT CW lasing VCSEL and also measured the laser characteristics, further more we designed a method to make more efficient in injection current and enhance the quality factor of cavity. Such a technique could be the more ideally structure for reduce threshold current in electrically injected GaN-based VCSEL.

致謝

又是鳳凰花開的時日，這兩年，要感謝的人實在太多太多，不是簡單的三言兩語可以感謝。 首先，要感謝王老師在每次報告中都和我們熱烈的討論，並且給予我們更廣闊的思考空間，郭老師總在我們實驗低潮的時候適時的給予我們鼓勵，尤其在最後最徬徨無助的時候。最後是盧老師，謝謝老師不厭其煩的和我們討論實驗細節及給予意見，有實驗室的三位大家長的照顧讓我在這兩年學到的不只是學識並且做事更有條理謹慎。直屬學長，宗鼎、士偉、博孝，謝謝你們總在我需要幫忙時伸出援手。明華、博閔、鏡學、李博，有你們強大的磊晶支援，才讓這篇論文能夠誕生，尤其博閔學長，謝謝你在百忙之中的高效率幫忙，讓實驗流程能夠更順利! 清華學長，沒有架子的學長，總是在實驗上給我最有效的建議。

我的好同學們，嗡嗡、阿菲、小昕、重卿、JO、大為、祥奇、阿吉…這兩年謝謝你們一路的陪伴，讓這兩年更有回憶，我們要出去打拼了，但千萬別忘記我們所擁有的一切甘苦回憶… 直屬的昀霖，VCSEL 的棒子終於接下去了，經過一年的共患難，相信你的表現一定能青出於藍。

在學習的這條路上，特別感謝二姨和五姨，有你們的照顧與關心讓政宏在這一路上走的很安穩順利。姿蓉，謝謝你這一路的陪伴，忍受我的脾氣和我一起成長，我們還有很長的路要一起前進。最後，要感謝我的父母，無怨無悔的付出、給予我最大的關心與支持，希望能讓你們以我為榮。

2010/07/28　　政宏

Contents

Abstract (in Chinese)..i

Abstract (in English)..ii

Acknowledgement……………………………………………………………………iii

Contents...v

Figure Contents…………………………………………………………………..vii

Chapter 1 Introduction

1.1 Wide band gap Ⅲ-Ⅴ materials……………………………………1

1.2 Semiconductor lasers………………………………………………2

Chapter 2 Operation principle of VCSEL

2.1 Optical characteristics of Fabry-Perot Resonator cavity

2.1.1 Distributed Bragg reflectors…………………………………....8

2.1.2 Quality Factor……………………………………………………11

2.1.3 Transverse Mode………………………………………………,,,12

2.2 Electrical characteristics of VCSELs

2.2.1 Threshold current…………………………………………………13

2.2.2 Output power and quantum efficiency……………………………16

2.2.3 Output Beam Characteristics……………………………………..17

Chapter3 Experimental principles and methods

3.1 Four point probe…………………………………………………………..18

3.2 Atomic force microscope (AFM)…………………………………………19

3.3 Photoluminescence spectroscopy (PL)……………………………………21

3.4 Electroluminescence spectroscopy (EL)…………………………………22

Chapter 4 Characteristics of electrical pumped GaN-based VCSELs

4.1 Previous work of our group

4.1.1Optical pumped VCSEL ……………………………………………24

4.1.2 CW lasing of current injected GaN-based VCSEL at 77k…..27

4.2 The design of electrical pumped VCSEL

4.2.1The reflectance and quality factor simulation with different ITO thickness……………………………………………………...31

4.2.2Design structure of electrical pumped device………………..34

4.3 Fabrication process of GaN-based VCSELs………………………...35

4.4 Characteristics of optically pumped GaN-based VCSELs…………..38

4.5 Characteristics of electrically pumped GaN-based VCSELs………..44

Chapter 5 Characteristics of electrically pumped GaN-based VCSELs with AlN Current Blocking Layer

5.1 Characteristics of AlN……………………………………………52

5.2 Fabrication of GaN-based VCSELs with AlN current blocking layer process

5.2.1 Initial clean and photolithography technique……………….55

5.2.2 Epitaxial flowchart ……………………………………….56

5.2.3 Process flowchart…………………………………………61

5-3 Characteristics of electrically pumped GaN-based VCSELs with AlN current blocking layer

5.3.1 The emission images of AlN VCSEL………………………64

5.3.2The I-V curves of AlN blocking layer and conventional VCSEL…………………………………………………….67

5.3.3The optical characteristics of AlN VCSEL…………………..68

5.4 Summary………………………………………………………69

Chapter 6 Conclusions……………………………………………………...70

Reference………………………. ……………………………………………...71

Figure content

Fig 1.1 the band-gap diagram of Ⅱ-Ⅵ and Ⅲ-Ⅴ group semiconductor materials

Fig 1.3 the schematic diagram of the VCSELs

Fig 1.4 the schematic diagram of three nitride based VCSELs structures

Fig. 2.1 Schematic diagrams of DBRs

Fig. 2.2 transmission pattern of a Fabry-Perot cavity in frequency domain

Fig. 3.1 four points probe

Fig 3.2 four point probe in NCTU Nano Facility Center

Fig. 3.3 Concept of AFM and the optical lever: (a) a cantilever touching a sample, (b) illustration of the meaning of "spring constant" as applied to cantilevers, (c) the optical lever. Scale drawing; the tube scanner measures 24 mm in diameter, while the cantilever is 100 μm long typically.

Fig. 3.4 The AFM feedback loop. A compensation network monitors the cantilever deflection and keeps it constant by adjusting the height of the sample (or cantilever).

Fig. 3.5 Interband transitions in photoluminescence system

Fig. 3.6 Spectrum of a blue electroluminescent light source. Peak wavelength is at 454 nanometers and the FWHM spectral bandwidth is quite wide at about 9 nm.

Fig. 4.1 The schematic diagram of the optical pumped VCSEL structure

Fig. 4.2 PL emission of the optical pumped VCSEL structure.

Fig. 4.3 The excitation energy - emission intensity curve (L-I)

Fig. 4.4 The laser emission spectrum with the increasing pumping energy.

Fig. 4.5 The schematic diagram of the current injected VCSEL structure

Fig. 4.6 Emission spectrum of the current injected VCSEL structure.

Fig.4.7The light output intensity vs injection current and current–voltage characteristics of GaN VCSEL

Fig. 4.8 The laser emission spectrum at different injection current levels measured at 77 K. Figure

Fig. 4.9 The simulation cavity structure

Figure 4.10The simulated reflectance spectra with different thickness of ITO

Figure4.11the simulated cavity mode with different thickness of ITO

Figure 4.12 The simulated quality factor with different thickness of ITO

Figure 4.13 Electric field intensity (red line) and refractive index (black line) as a function of the distance from top layer.

Fig 4.14 The schematic diagram of overall VCSELs process flowchart

Fib. 4.15 mesa

Fig 4.16 The ITO transparent conduct layer deposited on current aperture

Fig 4.17 The schematic diagram of completed electrical pumped VCSEL

Fig 4.18 The OM image of completed VCSEL device when current injects

Fig 4.19 The schematic diagram of the optical pumped VCSEL structure

Fig 4.20 The reflectance spectrum of bottom DBR

Fig. 4.21 The cross section SEM image of VCSEL cavity without upper DBR

Fig. 4.22 the PL and reflectance spectrum of VCSEL without upper DBR

Fig. 4.23 The reflectance spectrum of upper DBR

Fig. 4.24 The PL spectrum of optical pumped VCSEL with upper DBR

Fig. 4.25 The pumping energy density versus normalized intensity diagram

Fig. 4.26 The lasing spectrum of optical pumping VCSEL

Fig. 4-27(a)VCSEL full structure (b)turn on image at 2mA

Fig. 4-28(a)LIV curve at 300k (b) coupling factor from the log-log plot of L-I curve

Fig.4-29(a) emission spectra of our GaN-based VCSEL devices at current injection of 0.6 Ith, 1 Ith and 1.2 Ith, respectively (b) the measurement data at different angles and the solid curve is the fitting curve, (insert)the CCD image of a lasing spot size of about 2 μm in diameter.(c) the degree of polarization (DOP) of the laser beam

Fig.5.1 (a) AFM of three AlN temperature re-growth conditions

Fig.5.1 (b) PL after 2 steps re-growth

Fig.5.1.1 The overall diagram of VCSEL structure

Fig.5.2 The reflection spectrum of bottom DBR

Fig.5.3 The cross section SEM image of VCSEL cavity without upper DBR, the insert figure is the thickness of AlN layer.

Fig. 5.4 current aperture defined by SiO2.varying from 3um to 10um

Fig. 5.5 The p-GaN surface after liftoff SiO2 and the insert figure point out the pits on p-GaN

Fig5.6 The PL and reflectance spectrum of VCSEL without upperDBR

Fig. 5.7 Mesa etching and turn on image

Fig. 5.8 Passivation step Fig.5.9.1 ring shape ITO

Fig. 5.9.2 The ring shape ITO and CCD image

Fig. 5.9 Current lateral spreading by AlN current blocking, the white mark point out the 10um current aperture.

Fig. 5.10 n and p contact

Fig. 5.11 upper DBR

Fig. 5.12 Emission images of AlN VCSEL

Fig. 5.13 (a) The emission image of

aperture size of 3μm under high magnification CCD image

1896

(b)(c)(d)Beam-view on 3um aperture emission

Fig.5.14 I-V curve through this ring shape ITO, the VCSEL cavity become a more ideally resonate cavity than conventional VCSEL cavity with an absorption layer ITO.

Fig.5.15AlN VCSEL structure and CCD image of 10um aperture.

Fig. 5.16EL spectrum and structure of conventional and AlN CBL device

Chapter 1

Introduction

1.1 Wide-bandgap III-V materials

Wide-bandgap nitride materials have attracted great attention over past decade due to their promising potential for the applications of optoelectronic devices such as flat panel display, competing storage technologies, automobiles, general lighting, and biotechnology, and so on [1-4]. The III-N materials are synthesized mainly using the four kinds of atoms, gallium (Ga), nitride (N), aluminum (Al), and indium (In), to form the binary and ternary compounds such as GaN, InN, AlN, InxGa1-xN, and AlxGa1-xN etc. The bandgap of these materials cover a very wide range from 0.9eV to 6.1eV (figure 1.1), which implies the large band off-set in hetero-structure could be achieved in this material system. The large band off-set is very useful to confine carrier for the high-speed and high power electronic devices and light emitting devices [5]. Their wide-range bandgap also provide possibility of full-color emission because they cover red, green, and blue emission regions. This property further makes nitride materials important and important for the applications of full-color display or solid-state lighting. Furthermore, nitride materials still have lots of advantages such as high bond energy (~2.3eV), high saturation velocity (~2.7 $\times$ 10^4 cm/s), high breakdown field (~2 $\times$ 10^6 V/cm), and strong excitonic energy (>50meV)[6-7]. Although wurtzite nitride compounds have some unique properties such as piezoelectric field and spontaneous polarization which is harmful to the efficiency of light emitting devices, the material system still is a very strong candidate for the future optoelectronic applications due to their superior material properties.

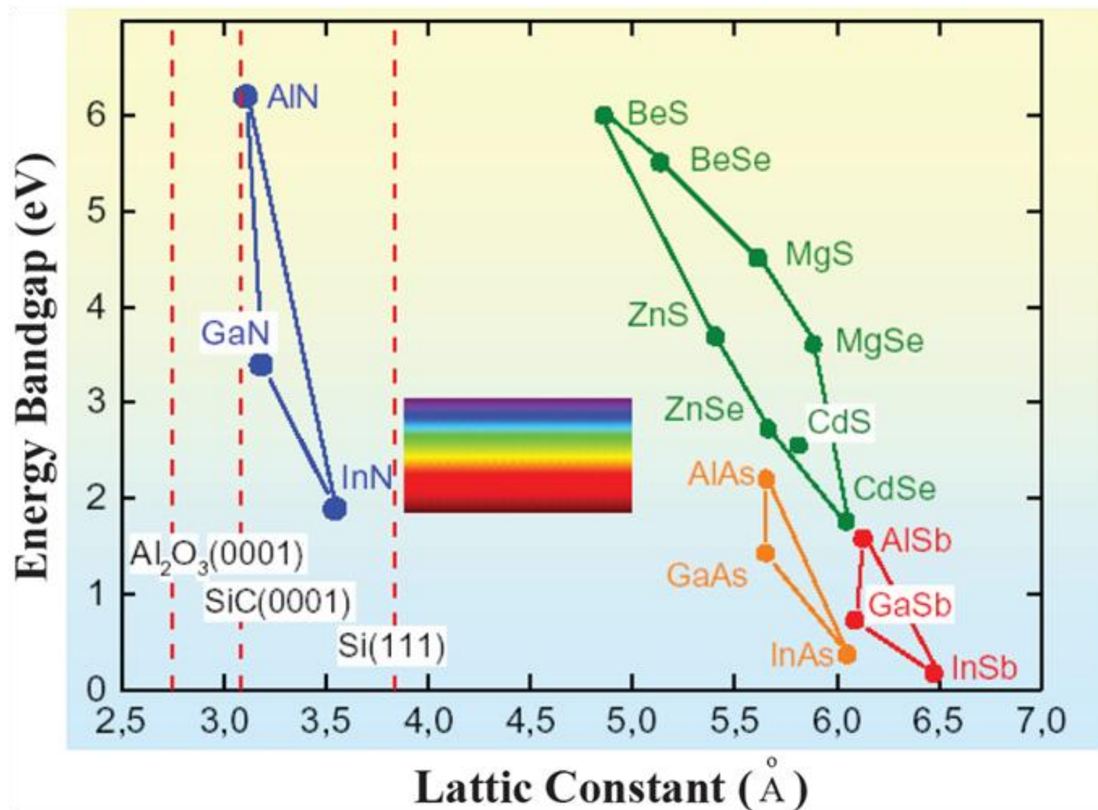

Fig 1.1 the band-gap diagram of Ⅱ-Ⅵ and Ⅲ-Ⅴ group semiconductor materials

1.2Vertical Surface Emitting Lasers

Although the optimization of the edge emitting laser keeps going, some properties of this kind of laser are unfavorable. One of those properties is its elliptic beam shape. On one hand, the coupling efficiency would be low as the elliptic beam is coupled into optical fiber (typically in the form of circular core). On the other hand, for the application of storage, the elliptic beam not only makes each writing pixel larger but also raises expenses for correcting light shape. Usually, this kind of laser shows slightly large divergence angle to be over ten degree. This also is disadvantageous to the projection. Furthermore, the side emitting laser devices also makes the testing of devices a tough task. The wafer should be cut into several

stripes (several laser devices on one strip) before the testing. For a commercial product, the complicated testing would result in a poor producing efficiency and be disadvantageous. Therefore, in order to have a superior laser device, K. Iga [16] demonstrated a new kind of laser diodes, vertical cavity surface emitting laser, in 1977. Vertical cavity surface emitting laser (VCSEL) is a vertical-emitting-type laser. It is formed by sandwiching a few-lambda cavity in a pair of reflectors, usually in the form of distributed Bragg reflector (DBR), with a very high reflectivity (>99.9%) (as shown in figure 1.3). In contrast to EELs, photons in the cavity of VCSEL are vertically in resonance and emit outside perpendicularly to the surface of the structure. This laser diode can have many advantageous properties than conventional edge emitting laser, such as circular beam shape, lower divergence angle, two-dimensional laser array possible, efficient testing, low threshold, and so on. Owing to these superior performances, VCSELs had become very attractive and started to be applied to the commercial products at long wavelength range. In fact, short-wavelength VCSELs are also very promising for the applications of storage, display, and projection. In particular, the use of two-dimensional arrays of blue VCSELs could further reduce the read-out time in high density optical storage and increase the scan speed in high-resolution laser printing technology [17].

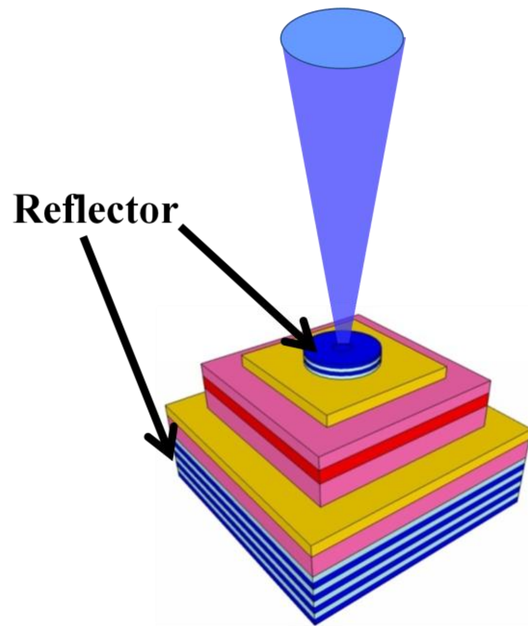

Fig 1.3 the schematic diagram of the VCSELs

In recent years, several efforts have been devoted to the realization of nitride-based VCSELs [18-27]. Currently, three kinds of structures were reported：

I. Fully epitaxial grown VCSEL structure

In 2005, J. F. Carlin [27] and E. Feltin [28] demonstrated the wholly epitaxial and high quality nitride-based micro-cavity (as shown in figure 1.4(a)) using metalorganic vapor phase epitaxy (MOVPE or MOCVD). They used the lattice-matched AlInN/GaN as the bottom and top reflectors to avoid cracks happened due to the accumulation of the strain after stacking large pairs of layers. The reflectivity of AlInN/GaN could be achieved as high as 99.4%. They showed the 3/2-lambda cavity emitted a very narrow emission with a linewidth of 0.52 nm, corresponding to a quality factor of ~800.

II. VCSEL structure with two dielectric mirrors

Compared to epitaxial grown reflectors, the fabrication of dielectric mirrors is relatively simple. Furthermore, the large index difference of dielectric mirrors makes them could easily have wide stop band (>50nm) and high reflectivity (>99%) by coating just few stacks of 1/4-lambda-thick layers. Therefore, using dielectric mirrors to accomplish nitride-based VCSELs had begun attractive. Song *et al.* [19], Tawara *et al.* [20] and J. T. Chu *et. al.* [22] successively reported the structure (as shown in figure 1.4(c)) after 2000. They employed some process techniques such as wafer bonding and laser lift-off to make dielectric mirrors be coated onto both sides of nitride-based cavity. They showed a micro-cavity could have a very high quality factor to be greater than 400 and achieve lasing action using optical pumping. In addition , Takashi Mukai *et al* [23] have demonstrated the CW lasing at room temperature in a GaN-based vertical-cavity surface-emitting laser (VCSEL) by current injection in 2008. Its optical cavity consisted of a 7λ-thick GaN semiconductor layer and an indium tin oxide layer for p-contact embedded between two SiO_2/Nb_2O_5 dielectric distributed Bragg reflectors. The threshold current of VCSEL is $13.9 kA/cm^2$ and the lasing wavelength is about 414nm. However, the fabrication techniques of this kind of VCSEL is relatively complicated, and its cavity length cannot be efficiently controlled due to polishing problems.

III. VCSEL structure with hybrid mirrors

The so-called hybrid mirrors are a combination of two different kinds of reflectors, for example, a dielectric mirror and an epitaxial reflector. Typically, the fabrication of this structure is to grow bottom reflector and cavity using MOCVD and then coat dielectric mirror to complete VCSEL structure (as shown in figure

1.4(b)). The hybrid-cavity nitride-based VCSEL\formed by the dielectric mirror and the epitaxially grown high-reflectivity GaN/$Al_xGa_{1-x}N$ DBR was reported earlier. In 1999, Someya et al. [18] used 43 pairs of $Al_{0.34}Ga_{0.66}N$/GaN as the bottom DBR and reported the lasing action at ~400nm. Then, Zhou et al [21] also employed a bottom DBR of 60 pairs $Al_{0.25}Ga_{0.75}N$/GaN and observed the lasing action at 383.2nm. Both these AlGaN/GaN DBR structures required large numbers of pairs due to the relatively low refractive index contrast between AlxGa1-xN and GaN. Therefore, recently some groups began to study the AlN/GaN for application in nitride VCSEL. The DBR structure using AlN/GaN has higher refractive index contrast ($\Delta n/n=0.16$)[29] that can achieve high reflectivity with relatively less numbers of pairs. It has wide stop band that can easily align with the active layer emission peak to achieve lasing action. However, the AlN/GaN combination also has relatively large lattice mismatch (~2.4%) and the difference in thermal expansion coefficients between GaN (5.59×10^{-6}/K) and AlN (4.2×10^{-6}/K) that tends to cause cracks in the epitaxial film during the growth of the AlN/GaN DBR structure and could result in the reduction of reflectivity and increase in scattering loss. With the mature of epitaxy techniques, the high-reflectivity AlN/GaN DBR structure with relatively smooth surface morphology has become possible with just twenty or thirty pairs [30]. In comparison of these three VCSELs, it doesn't require complicated process such as laser lift-off technique to complete a hybrid VCSEL device. This means the fabrication of such structure is stable and reliable comparing to other structures. Thus, the hybrid structure is more advantageous in the aspects of fabrication and commercialization In fact, the investigation of the characteristics of the GaN-based VCSELs has gradually attracted more attentions. Kako *et al.* [31] investigated the coupling efficiency of spontaneous emission (β) and the polarization property of the

nitride VCSEL and obtained a high β value of 1.6×10^{-2} and a strong linear polarization of 98%. Tawara *et al.* [20] also found a high β value of 10^{-2} in the nitride VCSEL with two dielectric mirrors. Honda *et al.* reported the estimation of high characteristics temperature of GaN-based VCSEL [32]. These all mean the development of nitride-based VCSEL and the understanding of the laser performance has become more and more important.

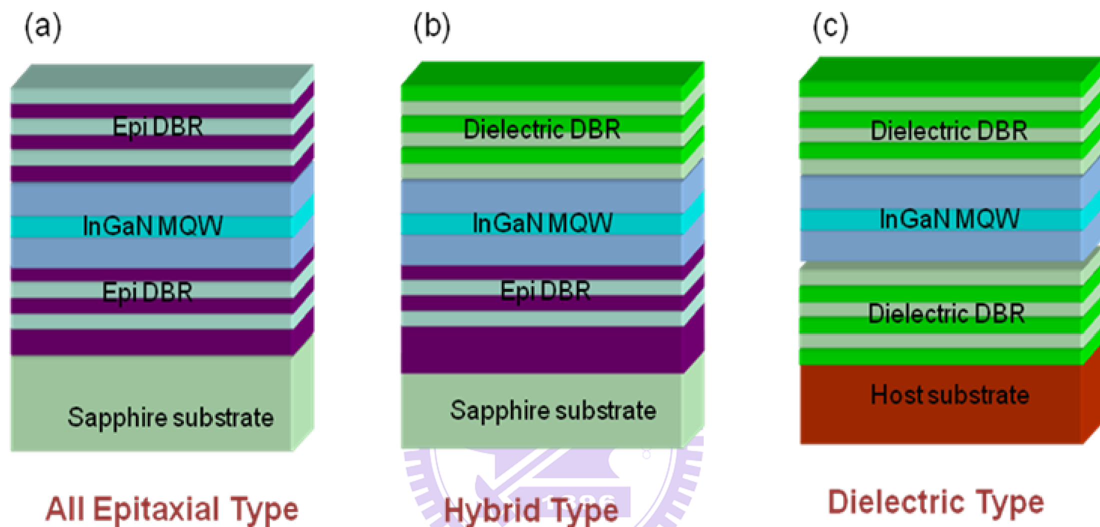

Fig 1.4 the schematic diagram of three nitride based VCSELs structures

Chapter 2

Operation principle of VCSEL

2.1 Optical characteristics of Fabry-Perot Resonator Cavity [33-37]

2.1.1 Distributed Bragg reflectors (DBR)

DBRs serve as high reflecting mirror in numerous optoelectronic and photonic devices such as VCSEL. There are many methods to analyze and design DBRs, and the matrix method is one of the popular one. The calculations of DBRs are entirely described in many optics books, and the derivation is a little too long to write in this thesis. Hence, we put it in simple to understand DBRs. Consider a distributed Bragg reflector consisting of m pairs of two dielectric, lossless materials with high- and low-refractive index n_H and n_L, as shown in Fig 2.1 The thickness of the two layers is assumed to be a quarter wave, that is, $L_1 = \lambda_B / 4n_H$ and $L_2 = \lambda_B / 4n_L$, where the λ_B is the Bragg wavelength.

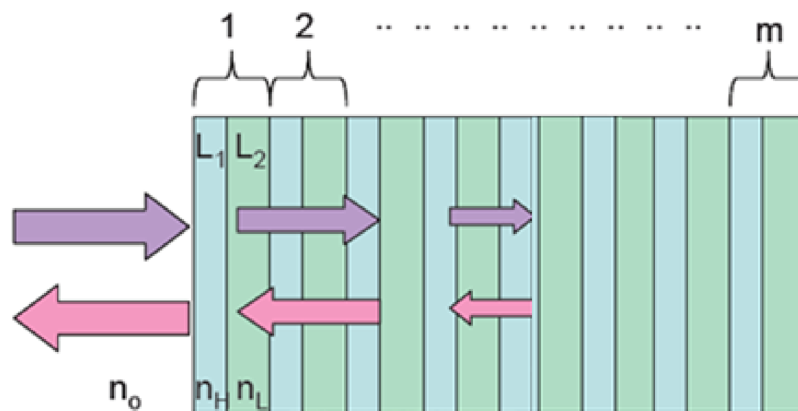

Figure 2.1 Schematic diagrams of DBRs

Multiple reflections at the interface of the DBR and constructive interference of the

multiple reflected waves increase the reflectivity with increasing number of pairs. The reflectivity has a maximum at the Bragg wavelength λ_B. The reflectivity of a DBR with m quarter wave pairs at the Bragg wavelength is given by

$$R = \frac{1 - \frac{n_s}{n_0}(\frac{n_L}{n_H})^{2p}}{1 + \frac{n_s}{n_0}(\frac{n_L}{n_H})^{2p}}$$

where the n_o and n_s are the refractive index of incident medium and substrate.

The high-reflectivity or stop band of a DBR depends on the difference in refractive index of the two constituent materials, Δn $(n_H - n_L)$. The spectral width of the stop band is given by

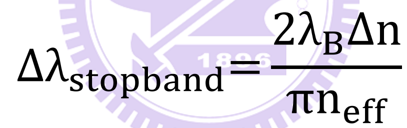

$$\Delta\lambda_{stopband} = \frac{2\lambda_B \Delta n}{\pi n_{eff}}$$

where neff is the effective refractive index of the mirror. It can be calculated by requiring the same optical path length normal to the layers for the DBR and the effective medium. The effective refractive index is then given by

$$n_{eff} = 2(\frac{1}{n_B} + \frac{1}{n_L})^2$$

The length of a cavity consisting of two metal mirrors is the physical distance between the two mirrors. For DBRs, the optical wave penetrates into the reflector by one or several quarter-wave pairs. Only a finite number out of the total number of

quarter-wave pairs are effective in reflecting the optical wave. The effective number of pairs seen by the wave electric field is given by

$$m_{eff} \sim \frac{1}{2}\frac{n_H+n_L}{n_H-n_L}\tanh\left(2m\frac{n_H-n_L}{n_H+n_L}\right) \sim$$

For very thick DBRs (m→∞) the tanh function approaches unity and one obtains

$$m_{eff} \approx \frac{1}{2}\frac{n_H+n_L}{n_H-n_L}$$

Also, the penetration depth is given by

$$Lpen = \frac{L_1+L_2}{4r}\tanh(2mr)$$

where r = (n1-n2)/ (n1+n2) is the amplitude reflection coefficient.

For a large number of pairs (m→∞), the penetration depth is given by

$$Lpen \sim \frac{L_1+L_2}{4r} = \frac{L_1+L_2}{4}\frac{n_H+n_L}{n_H-n_L}$$

Comparison of Eqs. (2.17) and (2.19) yields that

$$Lpen = \frac{1}{2}m_{eff}(L_1+L_2)$$

The factor of (1/2) in Eq. (2.20) is due to the fact that meff applies to effective number of periods seen by the electric field whereas Lpen applies to the optical power. The optical power is equal to the square of the electric field and hence it penetrates half as far into the mirror. The effective length of a cavity consisting of two DBRs is thus given by the sum of the thickness of the center region plus the two penetration depths into the DBRs.

2.1.2 Quality factor

Since the theory of Fabry-Perot cavity has been explained, we can talk about the finesse and the quality factor of resonant cavity. The cavity finesse, F, is defined as the ratio of the transmittance peak seperation (Δ ψ) to the transmittance full-width at half-maximum (δψ):

$$F = \frac{\Delta\phi}{\delta\phi} = \frac{\pi}{2\phi_{1/2}} = \frac{\pi}{1-\sqrt{R1R2}}$$

Figure 2.2 shows the transmission pattern of a Fabry-Perot cavity in frequency domain. The finesse of the cavity in the frequency is then given by F = νFSR/Δ ν.

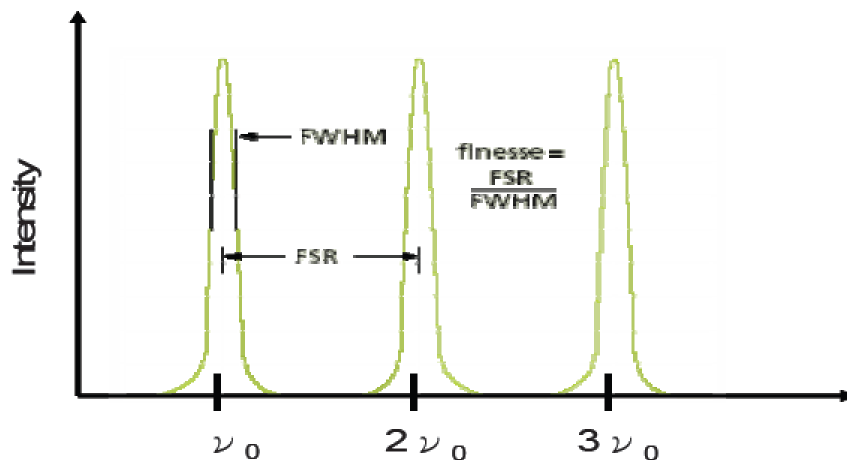

Figure 2.2 transmission pattern of a Fabry-Perot cavity in frequency domain

Besides the quality factor Q is also equal to λ/δλ, where δλ is the narrow emission linewidth around λ.

$$Q = \frac{\lambda}{\delta\lambda}$$

2.1.3 Transverse mode

The nature of the transverse optical confinement determines the possible lateral optical modes that might lase. Although VCSELs tend to lase in only a single axial

mode , because the DBR mirrors fill much of the cavity, lateral modes can exist for device diameters down to led than a micro. The losses explicitly discussed above were those of the fundamental lateral mode, although the general discussion may be applied to losses for higher-order modes as well. In fact, the higher-order modes tends to experience higher size-dependent optical losses than the fundamental mode, and this is why it is possible to observe single-mode operation in devices that have diameters of several microns

The transverse mode of gain-guided structures tends to vary with pumping level and thermal environment, and they are rather difficult to analyze analytically. However, the lateral modes of more strongly index-guided VCSELs with etched mesas or graded index dielectric waveguides, provided the Fresnel number is sufficiently large(F~10) so that significant diffraction does not occur in unguided sections. Then, the modes can be determined from normalized dispersion charts, generally used for optical fibers. In both the etched-mesa and dielectrically aperture cases, the effective lateral index profile can be determined by dividing the net change in optical path length over the cavity length by the cavity length. Thus, the assumed uniform waveguide has a lateral index roll-off given by

$$\delta n_1 = -\frac{\varphi_0(r)\lambda}{2\pi L} = -(n_o - n_{de})\zeta_{de}(r)t(r)/L$$

For a step index resulting from an abrupt dielectric aperture or an etched mesa, the aperture thickness $t(r < a) = 0$ and $t(r > a) = t$. For the etched-mesa VCSEL, t is taken to be L_{eff2} if the etch extends just through the top DBR mirror. For a tapered aperture, $t(r)$ varies with radius.

The change in the optical path length between the aperture and unapertured regions of the device gives rise to change in the longitudinal resonant wavelength with radius

[25]. The shift of the mode due to a change in a physical length, it can be applied general form:

$$\Delta\lambda(r) = \lambda\frac{\delta n_1(r)}{n_0}$$

Use Eq. (2.26) to determine the effective lateral index step is also possible, though it will not work if the shift becomes large than the longitudinal mode spacing or the mirror stop-band.

2.2 Electrical characteristics of VCSELs [38]

2.2.1 Threshold current

The threshold current Ith of surface-emitting lasers, which is common to semicondu-ctor lasers, in general, can be expressed with threshold current density Jth by the following equation:

$$I_{th} = \pi(D/2)^2 J_{th} = \frac{eN_{th}}{\eta_i \tau_s}V \sim \frac{eB_{eff}}{\eta_i \eta_{spon}} N_{th}^2 V \; \alpha \; V$$

where e is the electron charge, and V is the volume of the active region given by

$$V = \pi(D/2)^d$$

Thus, the threshold carrier density is given by

$$N_{th} = N_t + \frac{\alpha_a + \alpha_{d+}\alpha_m}{A_0 \xi}$$

Here, the parameters used are defined as follows.

α_a: Absorption loss coefficient averaged per unit length

α_d: Diffraction loss coefficient averaged per unit length

α_m: Mirror loss coefficient

A_0: Gain coefficient expressing differential gain A_0 =¼ dg/dN with g, optical gain per cm.

B_{eff} : Effective recombination coefficient

d: Total active layer thickness

D: Diameter of active region

L: Effective cavity length including spacing layers andpenetration layers of Bragg reflectors

N_t: Transparent carrier density

τ_p: Photon lifetime in cavity

τ_s: Recombination lifetime

ξ: Optical energy confinement factor

$$\xi = \xi_t \xi_l$$

ξ_t: Transverse confinement factor

ξ_l: Longitudinal confinement factor or filling factor relative to stripe lasers

$$\xi_l = \begin{cases} d/L & \text{for thick active layer} \\ 2d/L & \text{for thin active layer at the loop} \\ & \text{of optical standing wave} \end{cases}$$

ξ_i: Injection efficiency, sometimes referred to as internal efficiency

ξ_{spon}: Spontaneous emission efficiency

Parameter	Symbol	Stripe laser	VCSEL
Active layer area	S	3 x300 um^2	5 x 5 um^2
Active volume	V	60 um^3	0.07 um^3
Cavity length	L	300 um	1 um
Reflectivity	R_m	0.3	0.99– 0.999

Optical confinement	ξ	3%	4%
Optical confinement (transverse)	ξ_t	3 –5%	50–80%
Optical confinement (longitudinal)	ξ_l	50%	2 x1%x 3 (3QW)
Photon lifetime	ξ_p	1ps	1ps
Relaxation frequency (low current levels)	f_r	<5 GHz	>10 GHz

Table I Comparison of dimensions of stripe lasers and VCSELs

As seen from eq. (1), we recognize that it is essential to reduce the volume of the active region in order to decrease the threshold current. Assuming that the threshold carrier density does not change significantly, if we reduce the active volume, we can reduce the threshold until we encounter an increase in diffraction loss and diffusion of carriers. We compare the dimensions of surface-emitting lasers and conventional stripe geometry lasers, as shown in Table I. It is notable that the volume of VCSELs may be V ? 0:06 mm3, whereas that of stripe lasers remains V =60 um^3. This directly reflects the threshold currents in that the typical threshold of stripe lasers has a range of tens of mA or higher, but that for VCSELs can be made less than sub-mA order by a simple carrier confinement scheme such as proton bombardment. It could even be as low as several tens of microamperes by implementing sophisticated carrier and optical confinement structures, as will be introduced later. An early estimation of the threshold showed that the threshold current can be reduced proportionally to the square of the active region diameter. However, there should be a minimum value due to the decrease in the optical confinement factor that is defined

by the overlap of the optical mode field and the gain region when the diameter becomes small. In addition, the extreme reduction of volume, in particular, in the lateral direction, is limited by the optical and carrier losses due to optical scattering, diffraction of lightwaves, nonradiative carrier recombination, and other technical imperfections.

2.2.2 Output power and quantum efficiency

We also discuss the differential quantum efficiency of the VCSEL. If we use a nonabsorbing mirror for the front reflector, the differential quantum efficiency η_d from the front mirror is expressed, using α as

$$\eta_d = \frac{\alpha_m}{\alpha_a + \alpha_d + \alpha_m} = \eta_i \frac{(1/L)\ln(1/R_f)}{\alpha + (1/L)\ln(1/\sqrt{R_f R_r})}$$

where α is the total internal loss (= αa + αd), and Rf and Rr are front and rear mirror reflectivities, respectively. The optical power output is expressed by

$$P_0 = \begin{cases} \eta_d \eta_{spon} C E_g I & I \leqq I_{th} \\ \eta_d \eta_{spon} C E_g I_{th} + \eta_d \eta_{spon} (I - I_{th}) & I \geqq I_{th} \end{cases}$$

where Eg is the band-gap energy, C is the spontaneous emission factor, and I is the driving current. On the other hand, the power conversion efficiency η_P far above the threshold is given by

$$\eta_P = \frac{P_0}{V_b I} = \eta_d \frac{E_g}{V_b}\left(1 - \frac{I_{th}}{I}\right) \cong \eta_d \frac{E_g}{V_b} \cong \eta_d$$

where Vb is the bias voltage and the spontaneous component has been neglected. In the case of a surface-emitting laser, the threshold current can be very small, and therefore, the power conversion efficiency can be relatively high, i.e., higher than

50%. The power conversion efficiency is sometimes called the wall-plug efficiency.

2.2.3Output Beam Characteristics [34]

In a conventional edge-emitting diode laser, thin epitaxial layers must be used, which has the consequence that the width of optical mode in the direction perpendicular to the layers is always quite small (typically about two free-space wavelength). As a result, the emission angle in that direction is large (often of the order 30° or more). In the direction parallel to the layers, the width of the aperture is usually wider, thus yielding a noncircular beam. As the width of the aperture is widened beyond a few wavelengths, multiple transverse modes are excited and the beam become highly nonsymmetric and not longer diffraction limited. In contrast, a VCSEL with a circular aperture put out a circle beam, which simplifies the coupling into subsequent optical components (e.g., lenses and fibers). Moreover, a VCSEL with a single lateral mode can have an aperture several wavelengths across, thus yielding a narrower output beam than a conventional diode laser.

Chapter3
Experimental principles and methods

3.1 Four point probe

The 4-point probe setup consists of four equally spaced tungsten metal tips with finite radius. Each tip is supported by springs on the other end to minimize sample damage during probing. The four metal tips are part of an auto-mechanical stage which travels up and down during measurements. A high impedance current source is used to supply current through the outer two probes; a voltmeter measures the voltage across the inner two probes (See Fig3.1) to determine the sample resistivity. Typical probe spacing s ~ 1 mm. Fig 3.2 is the four point probe we used to sheet resistance measurement in NCTU NFC.

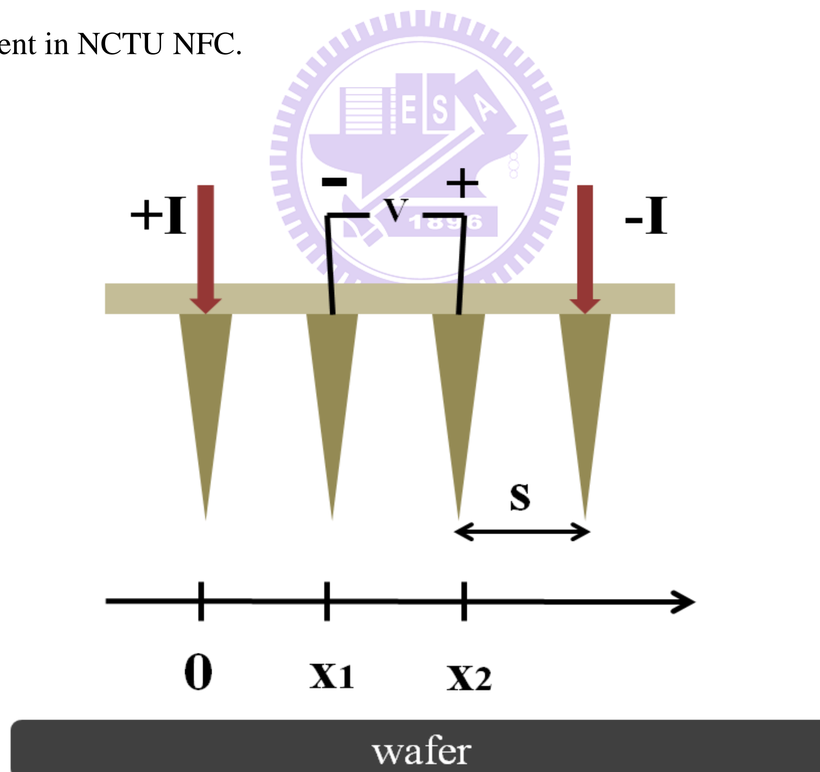

Fig. 3.1 four points probe

Fig 5.2 Schematic of 4-point probe configuration

Fig 3.2 four point probe in NCTU Nano Facility Center

3.2 AFM

The atomic force microscope (AFM) or scanning force microscope (SFM) was invented in 1986 by Binnig, Quate and Gerber. Like all other scanning probe microscopes, the AFM utilizes a sharp probe moving over the surface of a sample in a raster scan. In the case of the AFM, the probe is a tip on the end of a cantilever which bends in response to the force between the tip and the sample. The small probe-sample separation (on the order of the instrument's resolution) makes it possible to take measurements over a small area. To acquire an image the microscope raster-scans the probe over the sample while measuring the local property in question.

The resulting image resembles an image on a television screen in that both consist of many rows or lines of information placed one above the other. Unlike traditional microscopes, scanned-probe systems do not use lenses, so the size of the probe rather than diffraction effect generally limits their resolution. As shown in Fig. 3.3. AFM operates by measuring attractive or repulsive forces between a tip and the sample. In its repulsive "contact" mode, the instrument lightly touches a tip at the end of a leaf

spring or "cantilever" to the sample. As a raster-scan drags the tip over the sample, some sort of detection apparatus measures the vertical deflection of the cantilever, which indicates the local sample height. Thus, in contact mode the AFM measures hard-sphere repulsion forces between the tip and sample. In tapping mode, the AFM derives topographic images from measurements of attractive forces; the tip does not touch the sample.

The presence of a feedback loop is one of the subtler differences between AFMs and older stylus-based instruments such as record players and stylus profilometers. The AFM not only measures the force on the sample but also regulates it, allowing acquisition of images at very low forces. As shown in Fig. 3.4, the feedback loop consists of the tube scanner that controls the height of the entire sample; the cantilever and optical lever, which measures the local height of the sample; and a feedback circuit that attempts to keep the cantilever deflection constant by adjusting the voltage applied to the scanner. One point of interest: the faster the feedback loop can correct deviations of the cantilever deflection, the faster the AFM can acquire images; therefore, a well-constructed feedback loop is essential to microscope performance. AFM feedback loops tend to have a bandwidth of about 10 kHz, resulting in image acquisition time of about one minute.

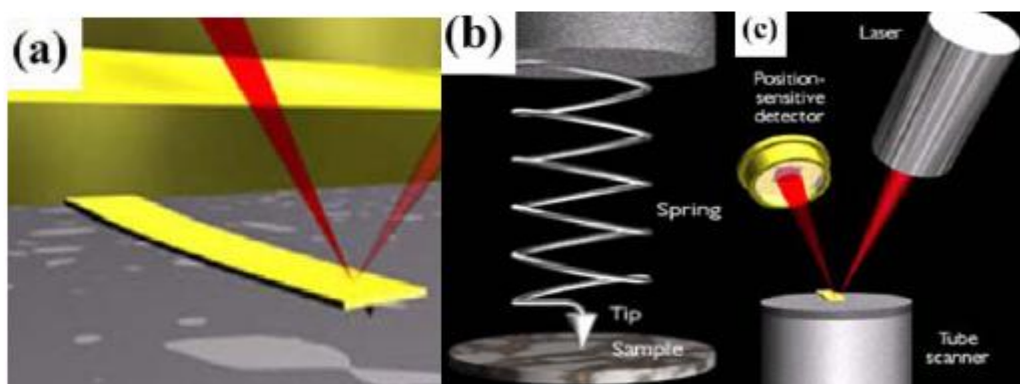

Fig. 3.3 Concept of AFM and the optical lever: (a) a cantilever touching a sample,

(b) illustration of the meaning of "spring constant" as applied to cantilevers, (c) the optical lever. Scale drawing; the tube scanner measures 24 mm in diameter, while the cantilever is 100 μm long typically.

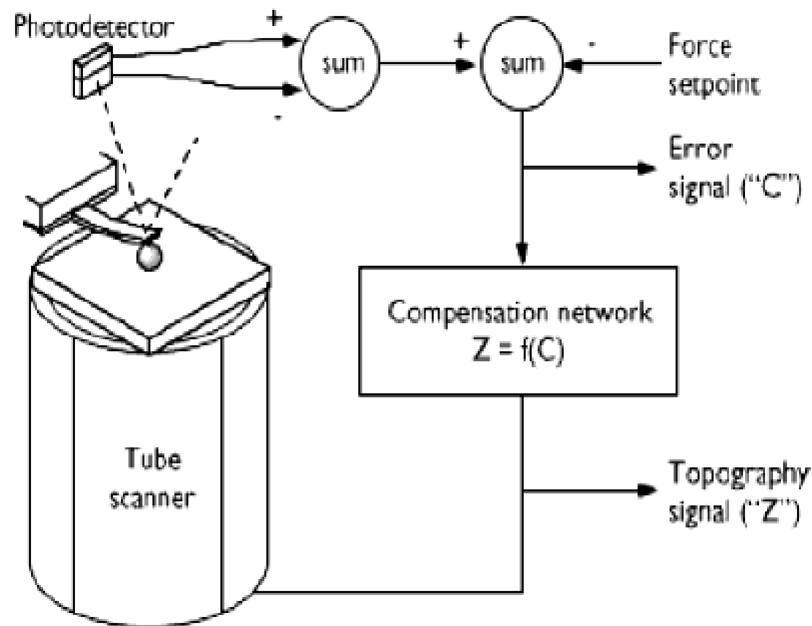

Fig. 3.4 The AFM feedback loop. A compensation network monitors the cantilever deflection and keeps it constant by adjusting the height of the sample (or cantilever).

3.3Photoluminescence spectroscopy(PL)

Photoluminescence characterization equipment generally uses the PL method to obtain the wavelength and intensity of the semiconductor material being analyzed. PL is the process of optical absorption of electrons in solids between an initial energy state Ei and a final energy state Ef. Excitation of an electron to Ef will leave Ei

unoccupied creating a hole. Absorption creates electron-hole pairs while luminescence is the process which occurs when electrons in excited states drop to a lower level emitting a photon ħw as shown in Fig. 3.5 The electron–hole recombination creates a photon which is also known as a radiative transition. Direct

gap materials are good light emitters and their optical properties are analyzed using this technique.

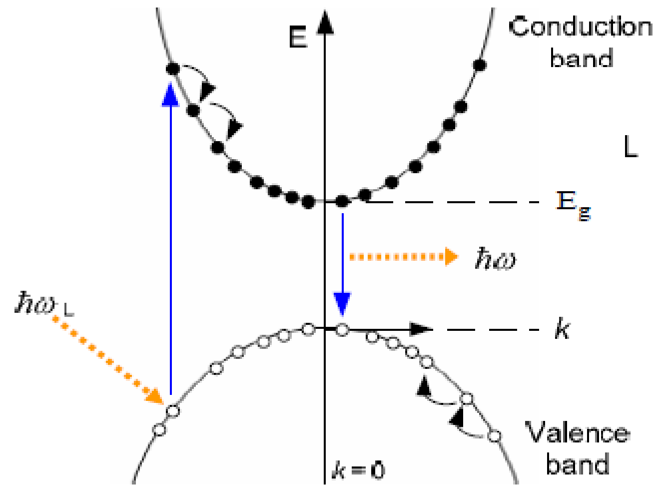

Fig. 3.5 Interband transitions in photoluminescence system

Photons are absorbed using an excitation source which is typically a laser. The frequency of the source ħwL must be greater than the energy gap Eg. The result is that electrons are injected into the conduction band and holes into the valence band. Electrons and holes are initially created in higher states within these bands but will rapidly relax to the bottom of their respective bands reaching their lowest energy state. Relaxation occurs by emitting phonons, for energy loses from the higher states, which obeys the conservation laws. The difference in energy between the two bands is Eg which is the energy gap, also known as the band gap. Luminescence occurs close to the band gap Eg, near $k = 0$. After excitation, both electrons and holes relax to their lowest energy states by emitting phonons.

3.4 Electroluminescence spectroscopy (EL)

As shown in Fig. 3.6, Electroluminescence (EL) is an optical phenomenon and electrical phenomenon in which a material emits light in response to an electric current passed through it, or to a strong electric field. This is distinct from light

emission resulting from heat (incandescence), chemical reaction (chemiluminescence), sound (sonoluminescence), or other mechanical action (mechanoluminescence). Electroluminescence is the result of radiative recombination of electrons and holes in a material (usually a semiconductor). The excited electrons release their energy as photons - light. Prior to recombination, electrons and holes are separated either as a result of doping of the material to form a p-n junction (in semiconductor electroluminescent devices such as LEDs), or through excitation by impact of high-energy electrons accelerated by a strong electric field (as with the phosphors in electroluminescent displays).

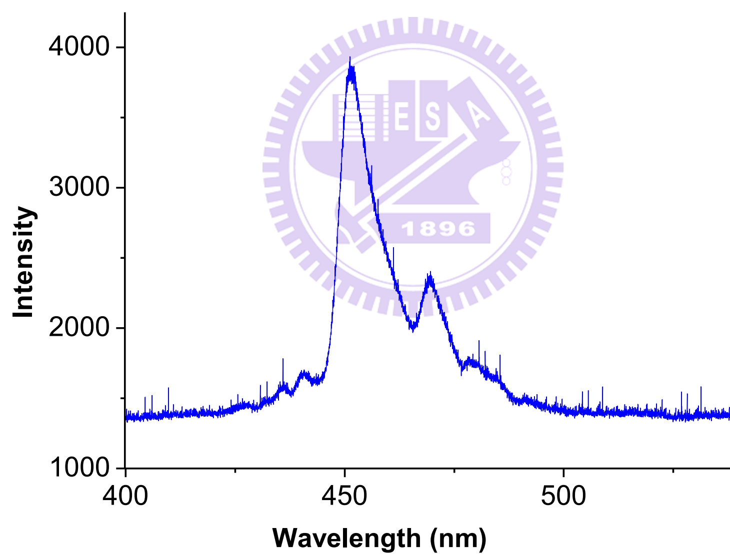

Fig. 3.6 Spectrum of a blue electroluminescent light source. Peak wavelength is at 454 nanometers and the FWHM spectral bandwidth is quite wide at about 9 nm.

Chapter 4
Characteristics of electrical pumped GaN-based VCSELs

4.1 Previous work of our group

4.1.1Optical pumped VCSEL

In our previous work, the characteristics of an optical pumped GaN-based VCSEL was successfully fabricated and investigated. The schematic diagram of the overall VCSEL structure are shown in the Fig. 4.1 . The hybrid DBR VCSELs structure is composed of 2-inch diameter c-plane sapphire , 2um thickness GaN buffer layer , 29 pairs AlN/GaN DBR , 5λ GaN cavity and 8 pairs Ta_2O_5/SiO_2 upper DBR. The reflectivity of lower and upper DBR are all about 99%. A narrow PL emission with full width at half maximum of 0.21nm corresponds to the cavity resonant mode at 454.3nm was observed, as shown in Figure 4.2. The cavity quality factor, estimated from the emission linewidth of 0.21nm, was about 2200. Figure 4.3 shows the laser action was achieved under the optical pumping at room temperature with a threshold pumping energy (E_{th}) of about 55 nJ corresponding to an energy density of 7.8 mJ/cm^2. A dominant laser emission line at 448.9 nm appearing above the threshold pumping energy is shown in the Fig.4.4.

Fig. 4.1 The schematic diagram of the optical pumped VCSEL structure

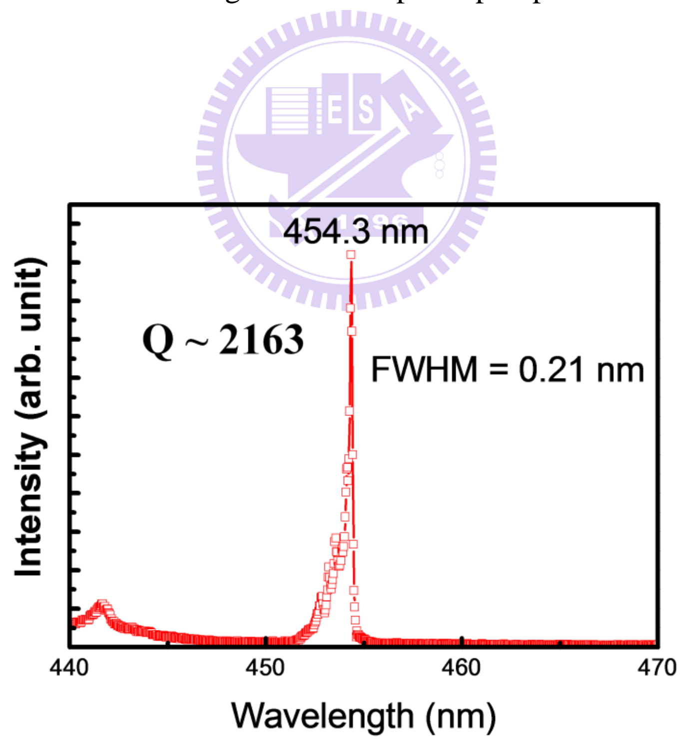

Fig. 4.2 PL emission of the optical pumped VCSEL structure.

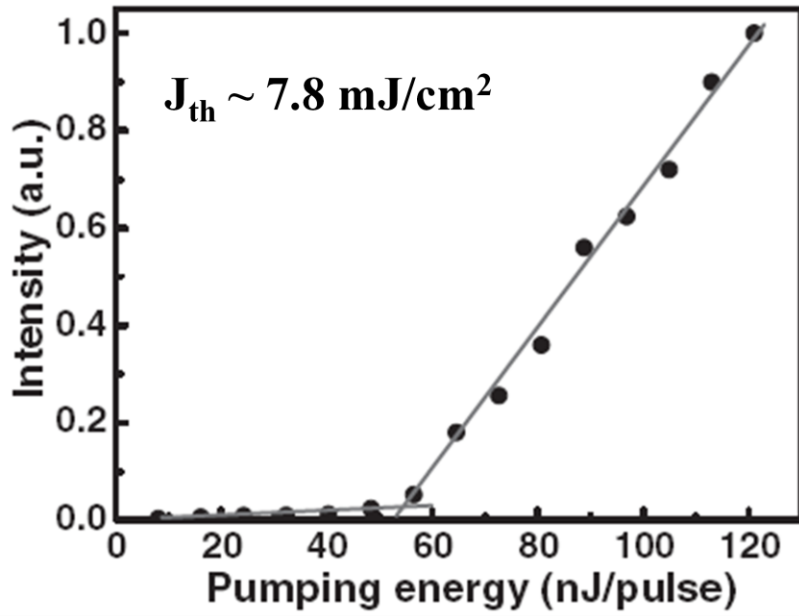

Fig. 4.3 The excitation energy - emission intensity curve (L-I)

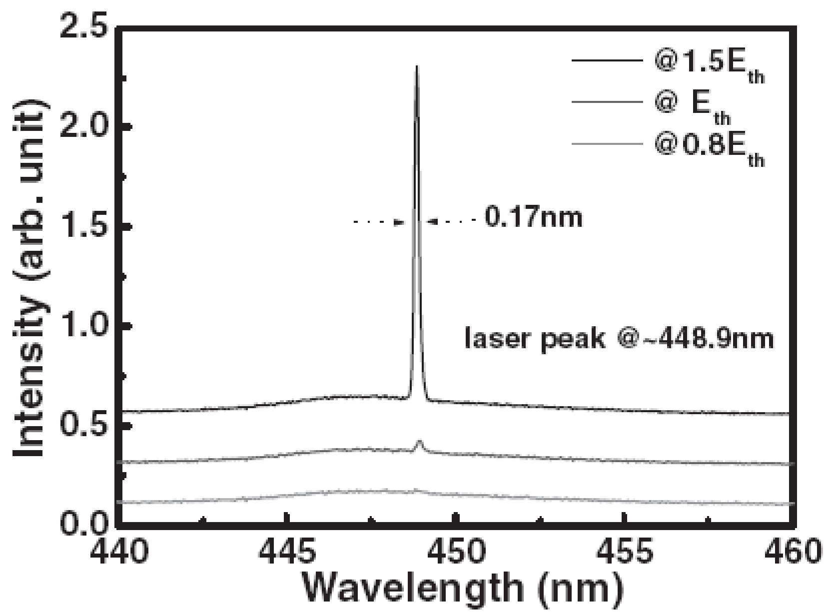

Fig. 4.4 The laser emission spectrum with the increasing pumping energy.

4.1.2 CW lasing of current injected GaN-based VCSEL at 77k

With the achievement of optically pumped GaN-based VCSEL, the realization of electrically-injected GaN-based VCSEL has become promising. Fig. 4.5 is the overall current injected VCSEL structure. The resonant cavity structure has an 0ne optical wavelength thickness ITO layer deposited on the p-type GaN layer compared with optical pumped cavity. The ITO layer can be used as a transparent conduct layer(TCL) and improve the current spreading problem resulting from low conductivity of p-GaN. In addition ,One optical wavelength thickness can match the resonance phase condition of microcavity and reach high transmittance(~98%) for ITO layer. However , we can find that the quality factor of electrically pumped cavity is about 900 from PL spectrum , as shown in Fig. 4.6. The value of quality factor is about half of the optical pumped result due to additional ITO absorption. We consider the loss of ITO maybe one of the main challenges for us to reach CW lasing in current injected VCSELs at room temperature.

In order to observe the lasing behavior in current injected VCSEL, we packaged our devices into TO can. The packaged VCSEL device was mounted inside a cryogenic chamber for testing under cw current injection condition using a cw current source at 77 K. Fig. 4.7 shows the light output power versus cw injection current and current-voltage characteristics of the VCSEL sample at 77 K. The laser light

output power showed a distinct threshold characteristic at the threshold current (*I*th) of about 1.4 mA and then was linearly increased with the injection current beyond the threshold. The threshold current density is estimated to be about 1.8 kA/cm^2 for a current injection aperture of 10 um in diameter, assuming the current is uniformly injected within the aperture. The lasing wavelength is 462.8nm with 0.15nm line width shown in Fig. 4.8. The inset of Fig3.8 is the CCD image of the spatial l emission pattern slightly below threshold. We believe the nonuniformity in the emission intensity across the aperture could be due to the In nonuniformity that creates a nonuniform spatial gain distribution in the emitting aperture as reported earlier[36]

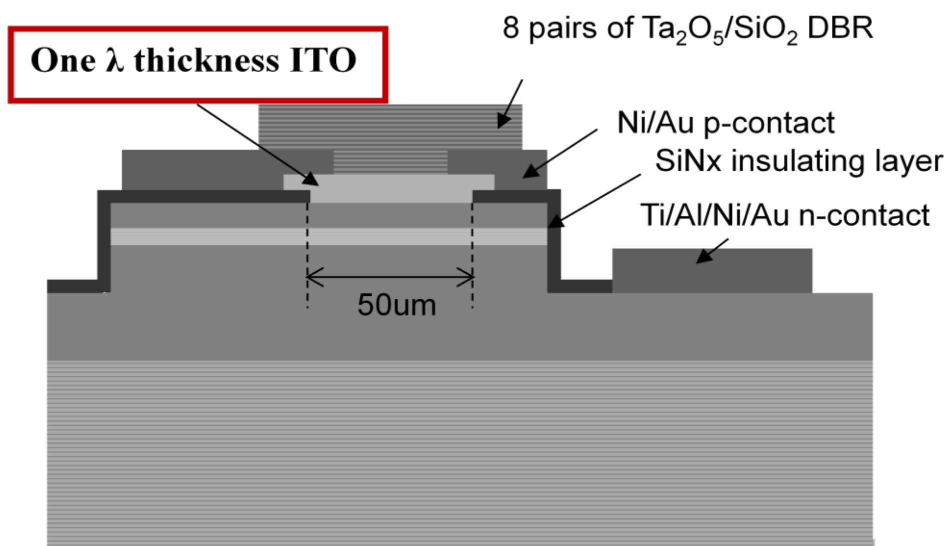

Fig. 4.5 The schematic diagram of the current injected VCSEL structure

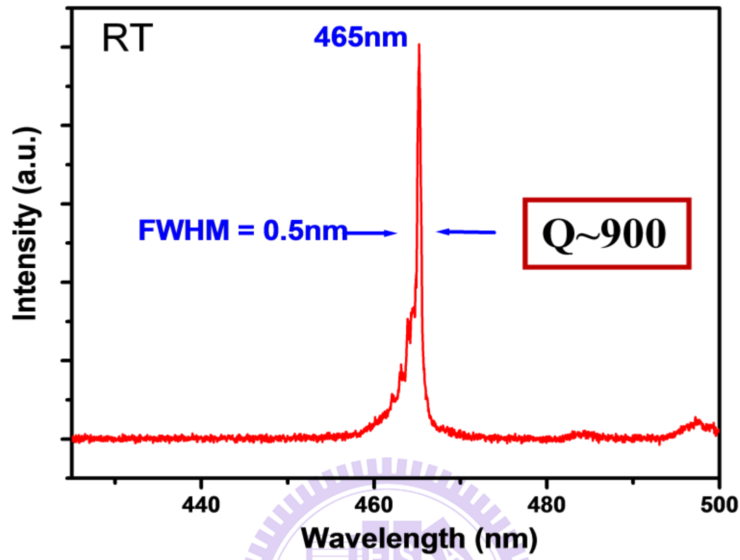

Fig. 4.6 Emission spectrum of the current injected VCSEL structure.

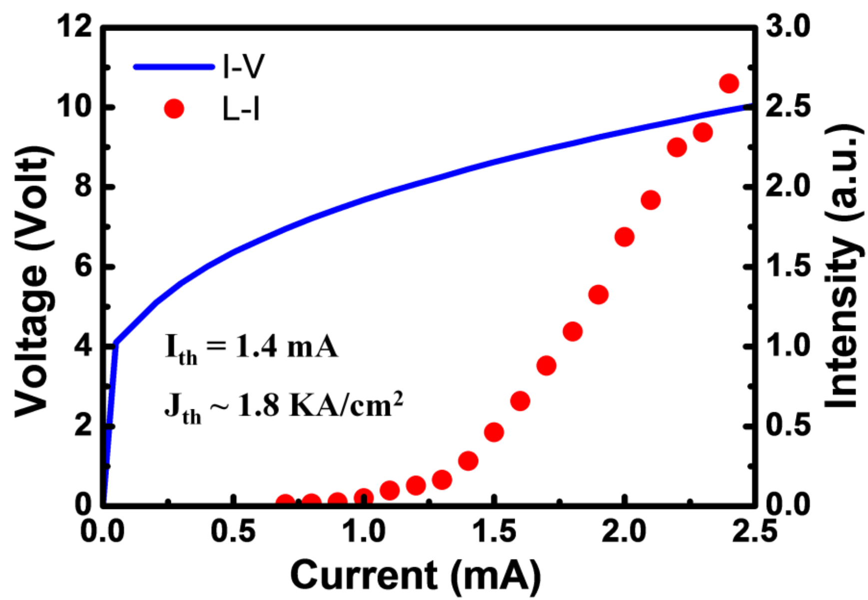

Fig. 4.7 The light output intensity vs injection current and current–voltage characteristics of GaN VCSEL

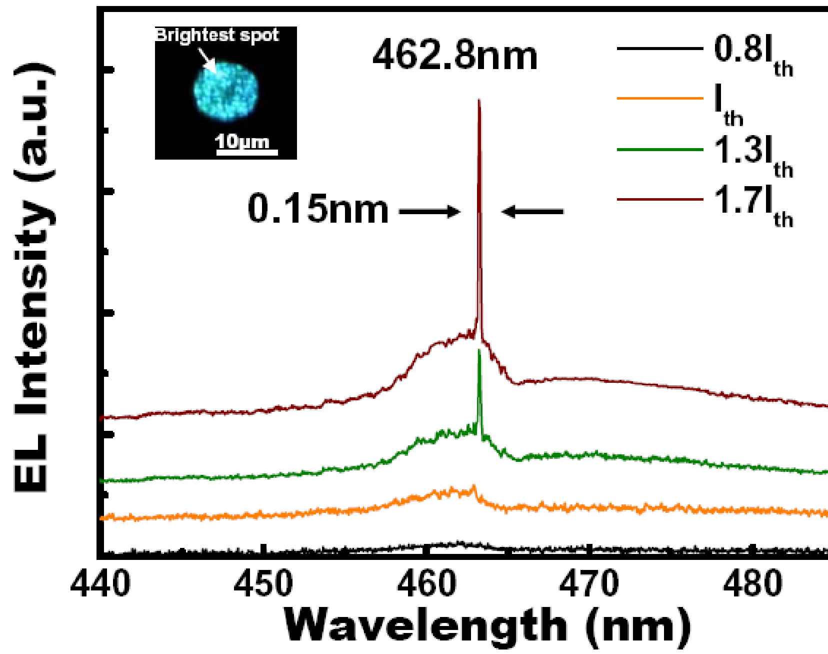

Fig. 4.8 The laser emission spectrum at different injection current levels measured at 77 K.

1896

4.2 The design of electrical pumped VCSEL

4.2.1The reflectance and quality factor simulation with different ITO thickness

So far, our group have fabricated and demonstrated the CW operation of an electrically pumped GaN-based VCSEL at 77 K. Next step, we should work toward the cw lasing of current injected devices at room temperature. In order to reach the goal, we try to reduce the loss of ITO so that the threshold current can also be lower at room temperature. In general, the thinner layer has the smaller absorption for the same material, so we would like to replace previous one optical wavelength thickness ITO with thinner ITO layer.

Figure show the simulation cavity structure with different ITO layer thickness from 0 nm, 30 nm, 120 nm, 210 nm, and 225 nm. Here, the 225nm-thick ITO layer stands for one optical wavelength thickness at 440nm. Owing to DBR reflectivity symmetry, the we chosen 18-pair AlN/GaN DBR. Figure is the simulated reflectance spectra under different ITO thickness. The dip positions in the reflectance spectra represent the cavity modes with different ITO thickness and the quality factor can be estimated from the linewidth of the dip. In

Figure, the cavity mode wavelength is the function of different ITO thickness. The cavity mode wavelength shifts to longer wavelength because of the longer cavity length, but the cavity mode wavelength would turn back to shorter wavelength when ITO thickness is thicker than 120nm due to the exceeding of the stop band region of the lower DBR. In this case, the cavity mode would jump to the $(m+1)_{th}$ mode from the m_{th} mode. Furthermore, the cavity mode also changes to multimode owing to longer cavity length and smaller mode spacing when ITO thickness is larger than 30nm. In Figure , the quality factor is about 700 using the cavity with a 225nm-thick

ITO layer, but this value is much lower than that without ITO layer of about 3300. If we consider the qualify factor of the cavity with a 30nm-thick ITO layer, the value of about 3100 is a little smaller than that with a 0nm-thick ITO layer but the structure with a ITO layer can be efficiently injected current in our electrical pumped VCSEL devices. Base on the simulation results and reality device requests, we can expect the 30nm ITO layer can efficiently reduce the loss and threshold current density of our VCSEL devices.

Figure 4.9 The simulation cavity structure

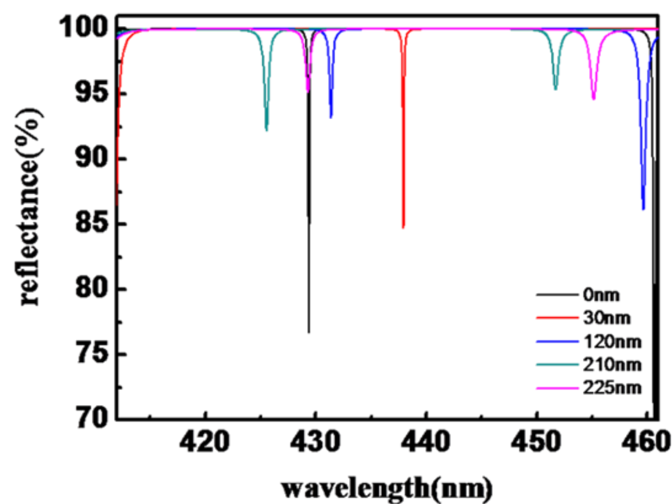

Figure 4.10The simulated reflectance spectra with different thickness of ITO

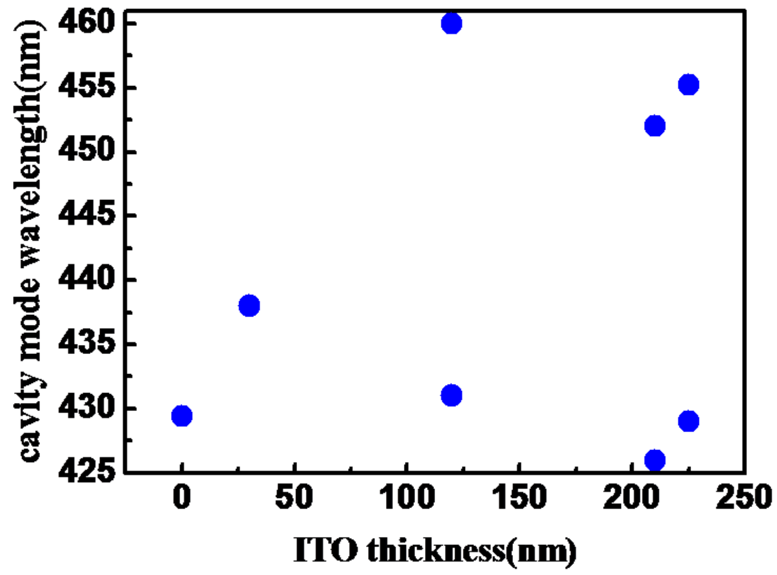

Figure4.11the simulated cavity mode with different thickness of ITO

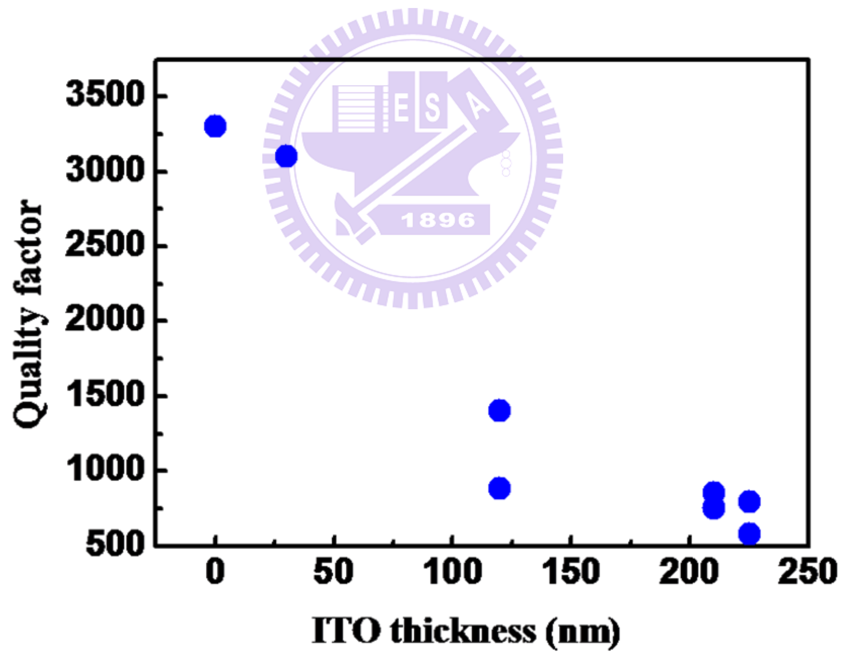

Figure 4.12 The simulated quality factor with different thickness of ITO

4.2.2Design structure of electrical pumped device

For a typical VCSEL, the cavity length is designed to be 1 lambda or 3/2 lambda, so the antinode of optical field and active region could be easily designed to match each other. However, in our design, the cavity length has been determined to be seven-λ (optical length), which correspond to a geometric thickness of about 1.1 μm, due to the consideration of device fabrication. The structure should compose of a top dielectric reflector, a ITO layer, a p-type GaN, MQWs, an n-type GaN, and a bottom nitride-based reflector. The optimal thickness of the ITO layer to be about 30 nm, the p-type InGaN to be about 2 nm, the p-type GaN to be about 110 nm, of the p-type AlGaN as a electron blocking layer to be about 24 nm, of 10-pair $In_{0.2}Ga_{0.8}N$(2.5 nm)/GaN(12.5nm) multi-quantum wells (MQWs) to be about 150 nm, and of the n-type GaN to be about 860 nm, and slightly modified these thicknesses to make the center of MQWs and the ITO layer at the anti-node and node of optical field, respectively. Figure shows the electric field intensity (EFI) and the refractive index as the functions of the distance from top layer. From the figure, it can be observed that a pronounced resonant enhancement of the electric field was built up in the active region. It suggests that the light could be amplified inside the resonant cavity and the more opportunity could be obtained to achieve laser operation.

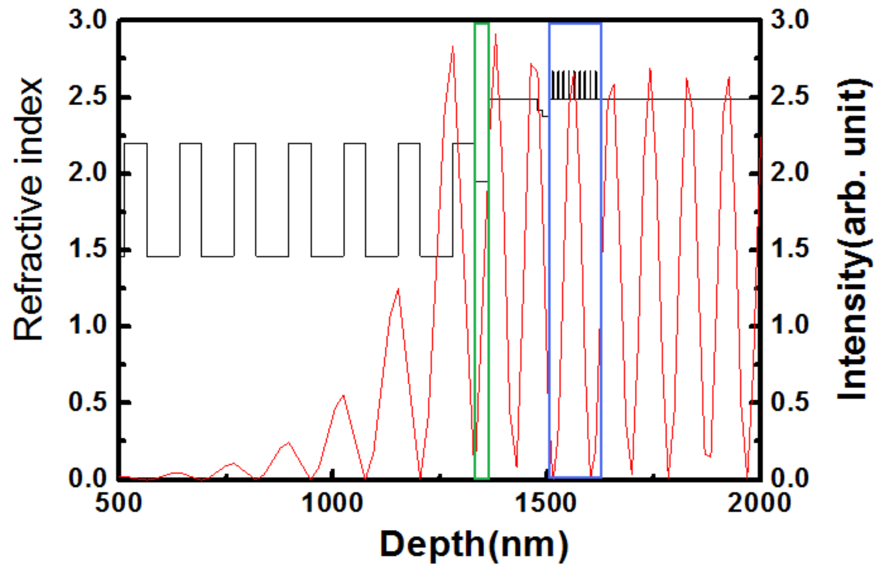

Figure 4.13 Electric field intensity (red line) and refractive index (black line) as a function of the distance from top layer.

4.3 Fabrication process of GaN-based VCSELs

To fabricate the VCSELs device on chip , we need to experience six process steps. Fig 4.14 is the schematic diagram of overall VCSELs process flowchart. In the beginning , SiNx mesa etching mask and ICP dry etching machine were used to define the mesa region . As shown in Fig 4.15, we check the electrically properties by probe station after mesa was finished. Then, 200nm SiNx layer was deposited by PECVD and patterned to form current confinement layer with effective current aperture varying from 15um to 40um. The four different structure ITO , which was mentioned earlier , were deposited individually by E-gun or sputter , and annealed at RTA system under nitrogen ambient. The ITO transparent conduct layer on a 40um current aperture after etching is shown in Fig 4.16. The Ti/Al/Ni/Au and Ni/Au contacts was deposited to serve as n-type and p-type electrode, respectively. The final step is deposition of 10pairs SiO_2/Ta_2O_5 dielectric DBR as upper mirror. The schematic diagram of completed electrical pumped VCSEL is shown in Fig 4.17 , and Fig4.18 is the OM image of VCSEL device with 5um metal aperture when current

injects.

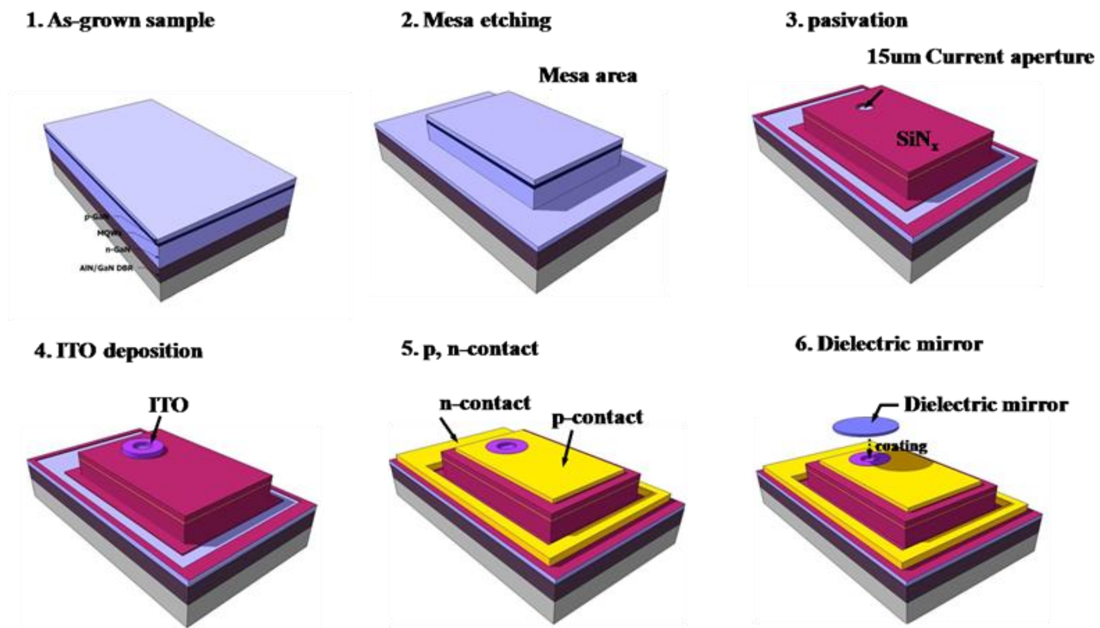

Fig 4.14 The schematic diagram of overall VCSELs process flowchart

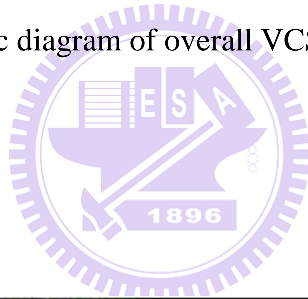

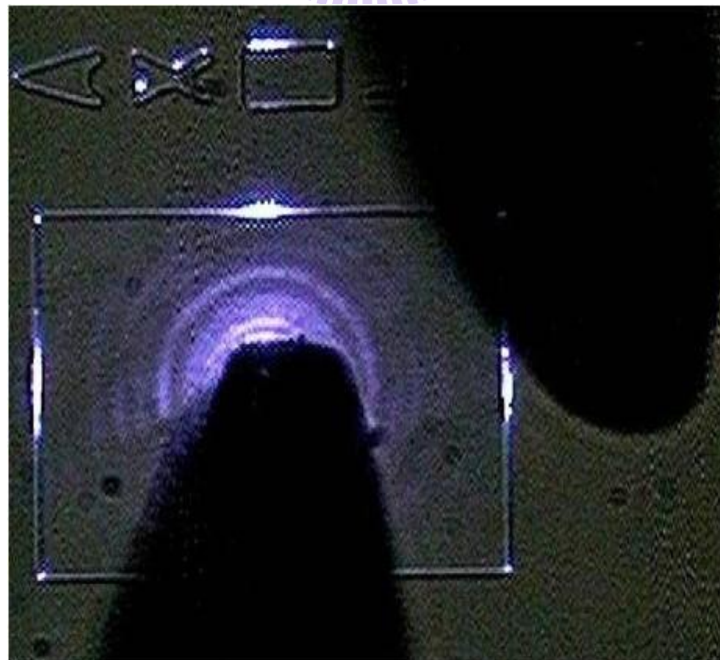

Fig 4.15 The defined mesa of first step was measured by probe station

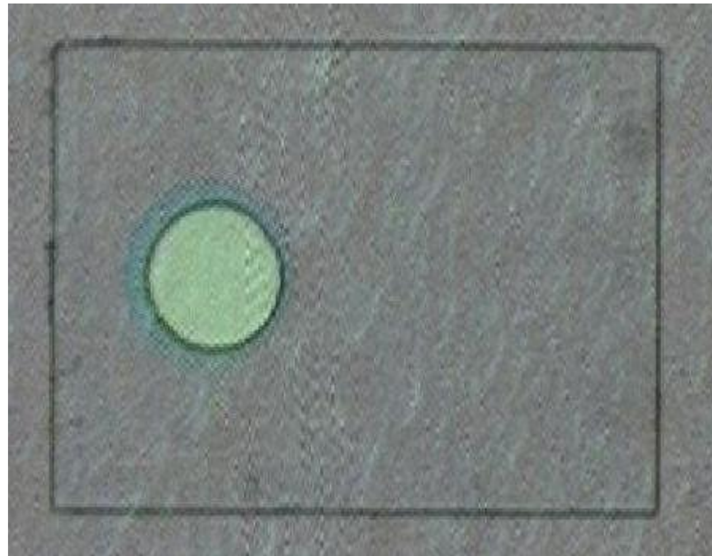

Fig 4.16 The ITO transparent conduct layer deposited on current aperture

E S A
1896

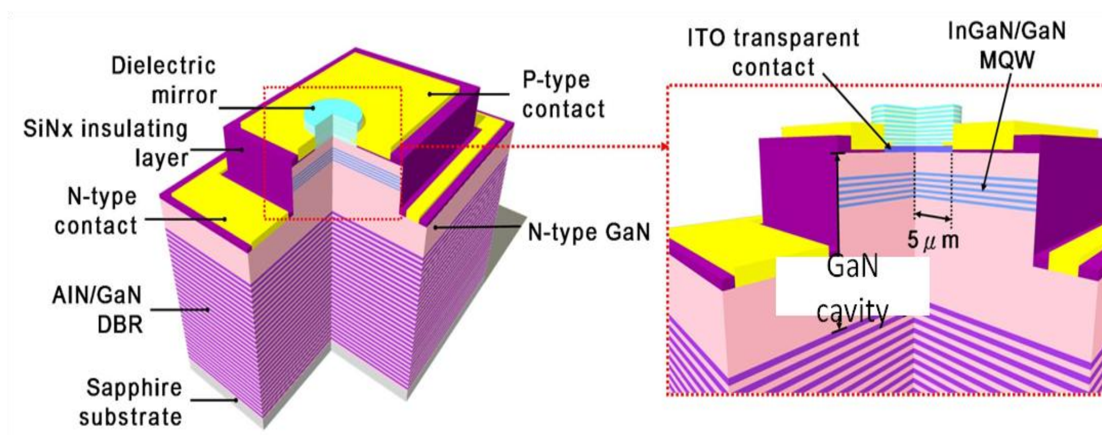

Fig 4.17 The schematic diagram of completed electrical pumped VCSEL

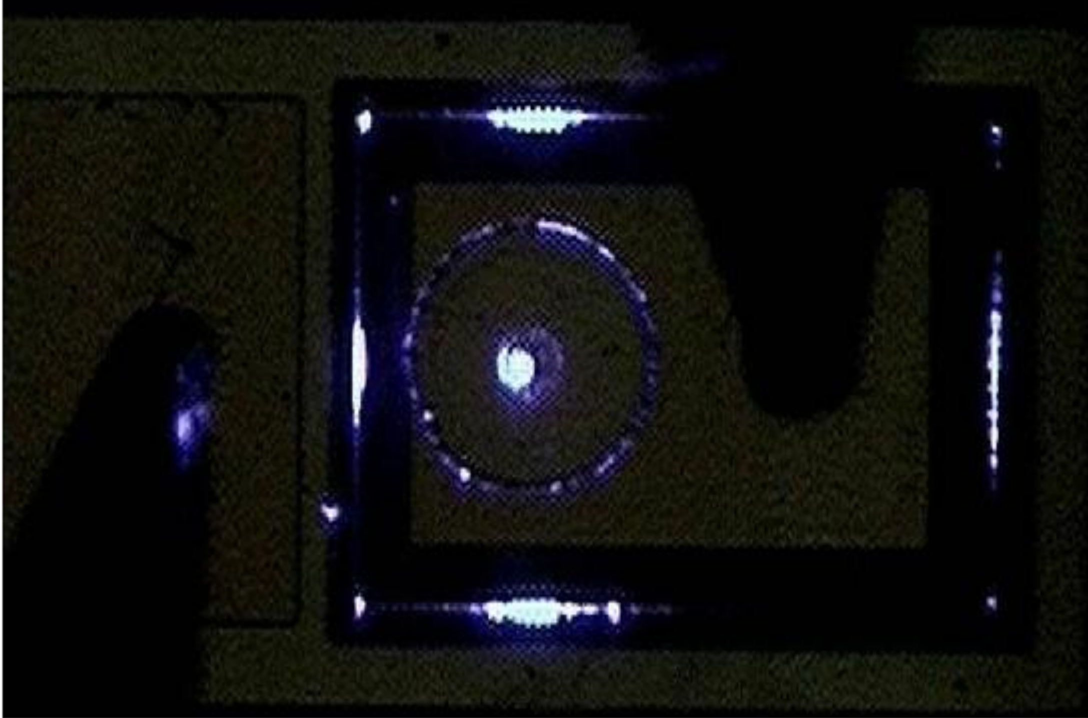

Fig 4.18 The OM image of completed VCSEL device when current injects

4-4 Characteristics of optically pumped GaN-based VCSELs

The overall optical pumped GaN VCSEL structure is shown in Fig 4.19 The mirocavity and bottom DBR structure are grown in a vertical-type MOCVD system (EMCORE D75), which can hold one 2-inch sapphire wafer. The nitride-based DBR used in the experiment is the stacks of 29-pair AlN/GaN layers with insertion of the AlN/GaN super-lattice (SL). The super-lattice in structure is inserted for releasing strain during the growth of AlN/GaN DBR to further improve interface and raise reflectivity of the DBR. Fig4.20 is the reflectance spectrum of bottom DBR, and there is a high reflectivity (~99.3%) at 440nm. The stop band of bottom DBR is as wide as about 20nm.

Then, a micro-cavity formed by a p-n junction was grown following the growth of the DBR structure. The micro-cavity composed of about 860-nm-thick n-type GaN, a

ten pairs $In_{0.2}Ga_{0.8}N/GaN$ (2.5 nm/7.5 nm) MQW, 24nm AlGaN electron blocking layer, a 115-nm-thick p-type GaN and 2nm InGaN layer. The cavity length is about 7-λ in optical length. The 2nm InGaN layer is used for reduction the Schottky barrier height between ITO and p type GaN layer[37], and it can also improve current spreading when current inject. The SEM cross-section image is shown in Fig4.21 , and Fig4.22 are the PL spectrum and reflectance spectrum of VCSEL sample without upper DBR. Obviously, the cavity mode is at about 435nm.

The final process to complete a VCSEL is the deposition of a dielectric mirror. The dielectric mirror in the experiment, an eight pairs Ta_2O_5/SiO_2 DBR, was deposited using the electron beam evaporation. The dielectric mirror was coated onto as-grown sample surface in an O2 ambient at the controlled temperature about 150℃. The reflectivity spectrum of the dielectric mirror was measured as shown in Fig 4.23 The Ta_2O_5/SiO_2 DBR shows a very high reflectivity as high as 99% centered at 450 nm with a wide stop-band of about 100 nm.

Fig4.24 is the PL spectrum of GaN-based VCSEL with bottom and upper DBR. The cavity mode wavelength is about 440nm with a 0.24nm linewidth , and the quality factor estimated from PL spectrum is as high as 1900. The lasing behavior can be observed under optical pumping at room temperature in Fig4.25 . The threshold pumping energy density is about $3.3mJ/cm^2$, and this lower value compared with the previous result of our group represents the improvement of epitaxial quality, so that the internal loss and threshold energy density is reduced. Fig4.26 shows the lasing spectrum above the threshold condition, and the lasing wavelength is 438nm with a 0.15nm linewidth.

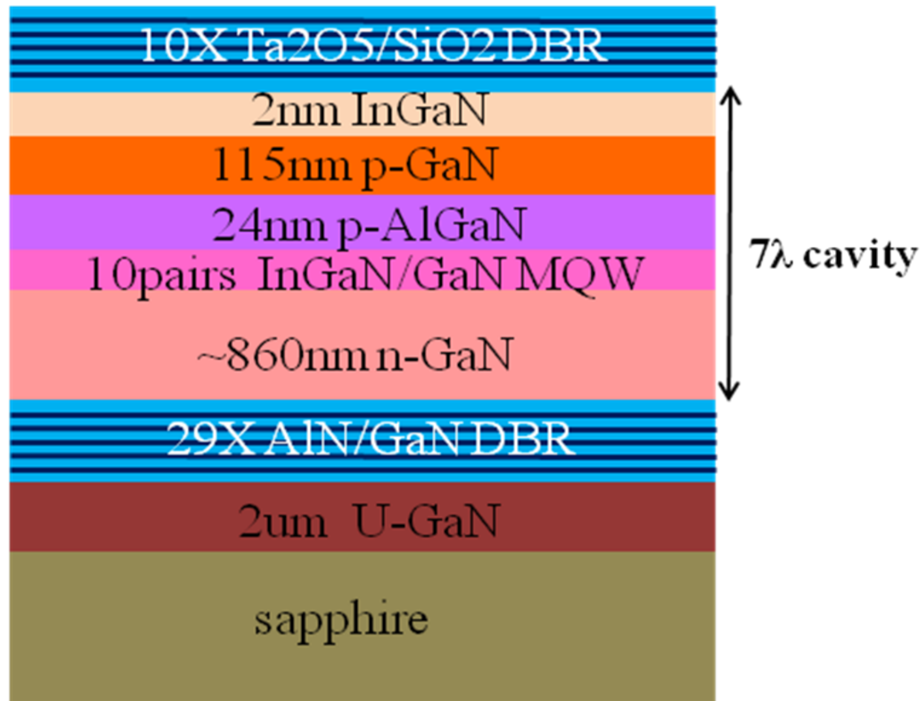

Fig 4.19 The schematic diagram of the optical pumped VCSEL structure

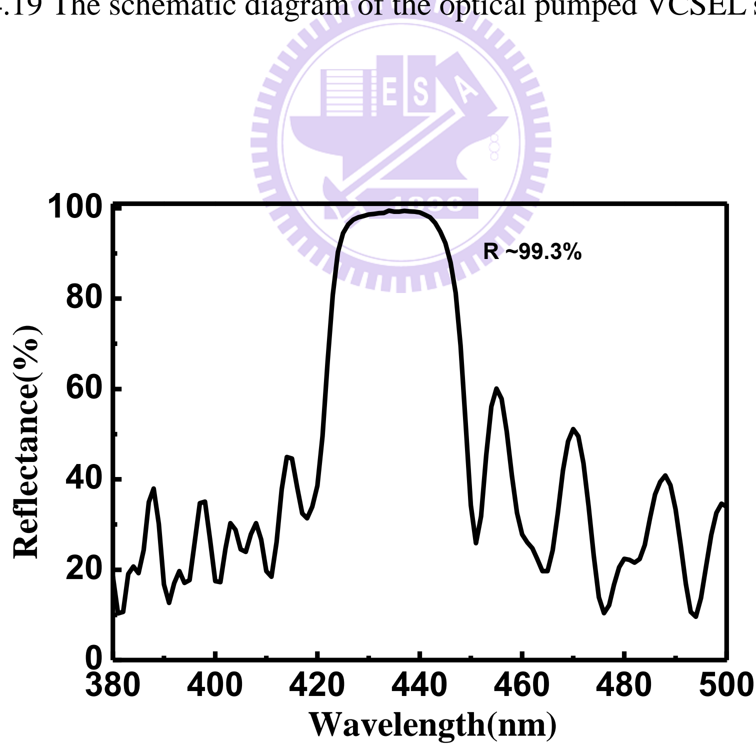

Fig 4.20The reflectance spectrum of bottom DBR

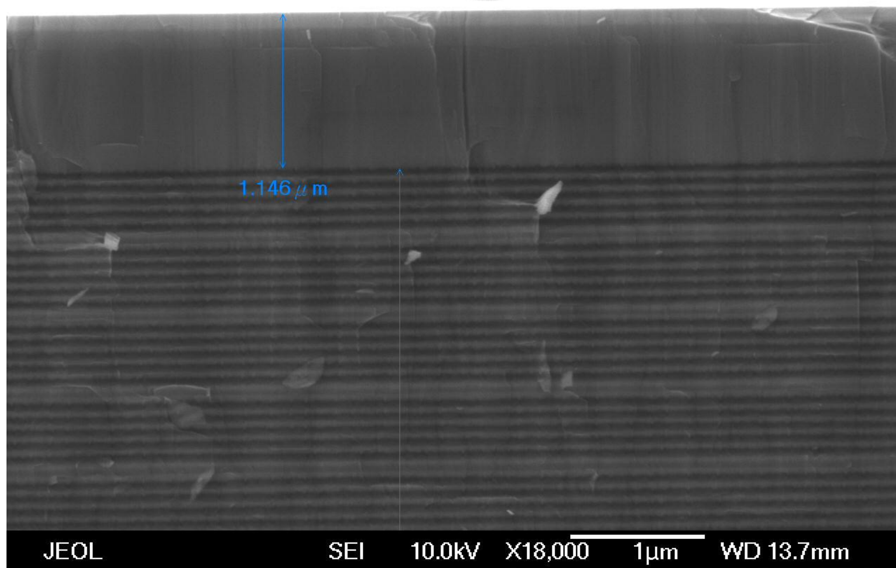

Fig 4.21 The cross section SEM image of VCSEL cavity without upper DBR

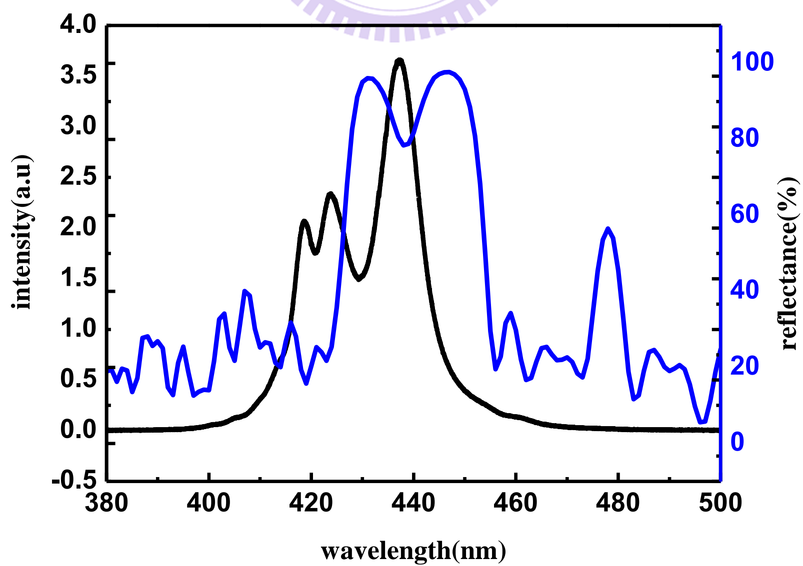

Fig 4.22 the PL and reflectance spectrum of VCSEL without upper DBR

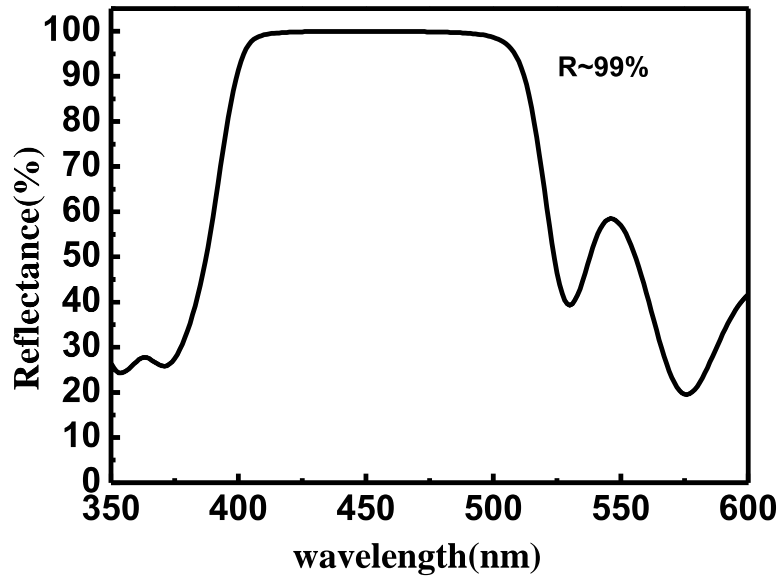

Fig 4.23 The reflectance spectrum of upper DBR

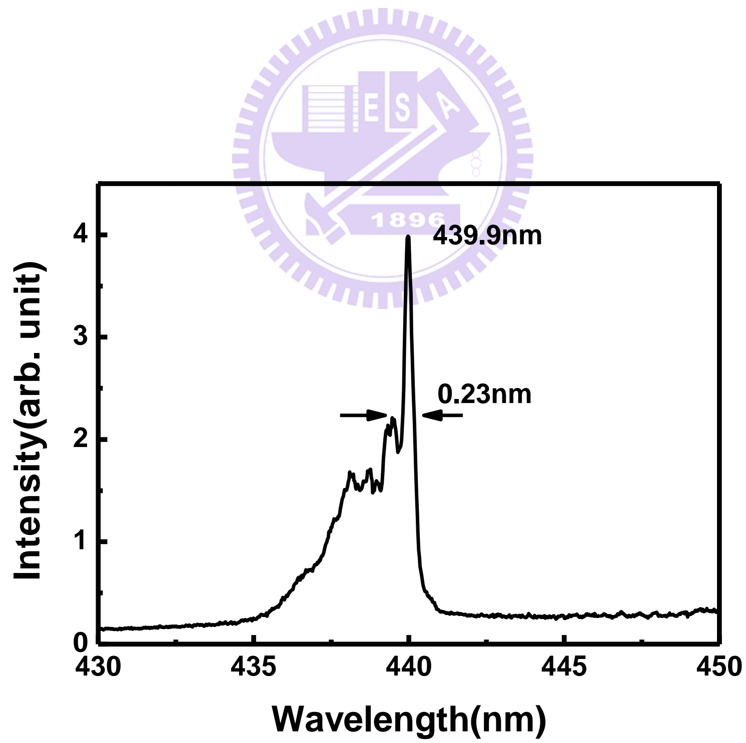

Fig 4.24 The PL spectrum of optical pumped VCSEL with upper DBR

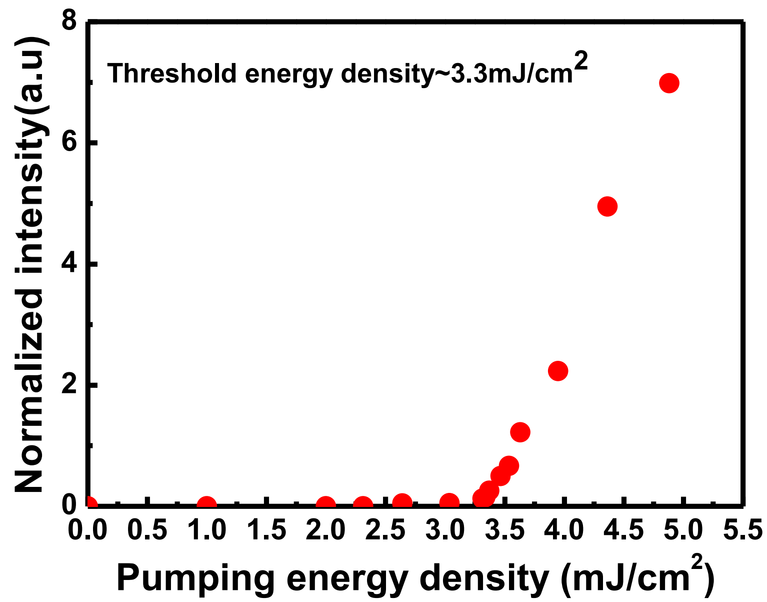

Fig 4.25 The pumping energy density versus normalized intensity diagram

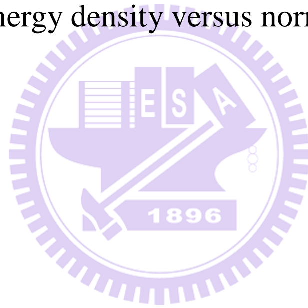

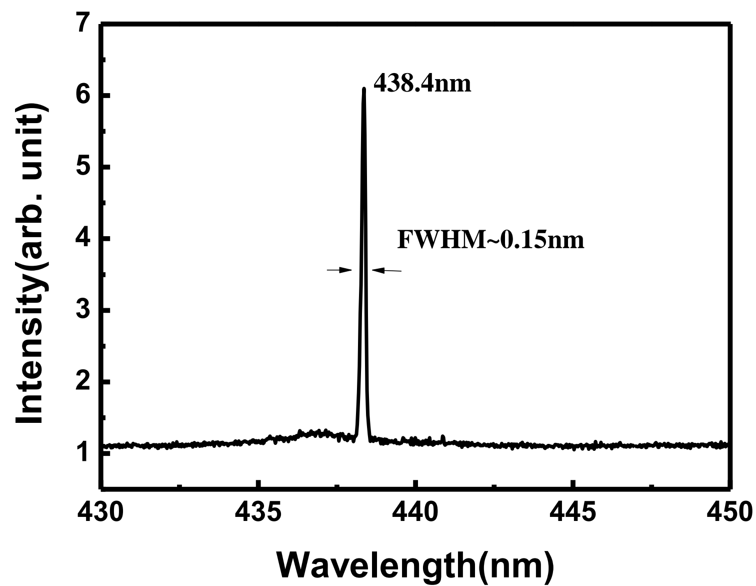

Fig 4.26 The lasing spectrum of optical pumping VCSEL

4-5 Characteristics of electrically pumped GaN-based VCSELs

We report the demonstration of the CW laser action on GaN-based vertical cavity surface emitting lasers (VCSEL) at room temperature. The laser structure consists of a 10-pair Ta_2O_5/SiO_2 distributed Bragg reflector (DBfR), a 7λ-thick optical cavity, 10 pairs InGaN/GaN multi-quantum wells with an AlGaN electron blocking layer, and a 29-pair AlN/GaN DBR. The laser has a threshold current of about 9.7 mA corresponding to the current density of about 12.4 kA/cm^2 and a turn-on voltage about 4.3 V at 300K. The lasing wavelength was 412 nm with a linewidth of about 0.5 nm. A spontaneous emission coupling efficiency factor of about 5×10^{-3} and the degree of polarization of about 55% were measured, respectively. The laser beam has a narrow divergence angle of about 8°.

GaN-based materials have attracted a great attention since the early 1990s due to the wide direct band gap and the promising potential for the optoelectronic devices such as light emitting diodes (LEDs) and laser diodes (LDs) [38-39]. So far, GaN-based edge emitting lasers have been demonstrated and applied in commercial products for high density optical storage applications. However, the vertical cavity surface emitting lasers (VCSELs), with superior characteristics such as the single longitudinal mode emission, low divergence angle, and array capability, are still under development and currently gaining much attention. Optically pumped GaN-based VCSELs have been reported by using different kinds of optical cavity structures, such as dielectric distributed Bragg reflectors (DBR) VCSELs with cavities consisting of dielectric top and bottom DBRs [40], and hybrid DBR VCSELs with cavities consisting of epitaxially grown nitride bottom DBRs and dielectric top DBRs [41]. We have recently demonstrated the CW current injection of GaN-based VCSEL with

hybrid mirrors at 77K in 2008 [42]. Subsequently, the room temperature operation of GaN-based VCSEL devices was reported using optical cavities sandwiched by double dielectric DBRs [43,44]. The major improvements of their devices to achieve room temperature operation are by using a thinner transparent conducting layer of about 50 nm to reduce the internal optical loss and by using the GaN substrate to ensure the good crystal quality of active layers. However, to form VCSELs with double dielectric DBRs required complex fabrication process, such as laser lift-off or elaborated polishing and bonding process [45]. In this paper, we report the achievement of CW room temperature lasing with hybrid DBR cavity and a thin Indium-Tin-Oxide (ITO) layer of 30 nm as the transparent conducting layer combining with a thin heavily doped p-type InGaN contact layer to reduce the optical loss while maintaining good current spreading capability. Moreover, we inserted an AlGaN electric blocking layer on the top of the InGaN multiple quantum well (MQW) to prevent the carrier overflow [46]. The lasing characteristics such as laser output power and device voltage versus injected current characteristics, degree of polarization, divergence angle, and spontaneous emission coupling factor have been measured and investigated.

Fig. 4-27(a) shows the schematic diagram of the whole GaN-based VCSEL structure. In the structure, the positions of the ITO layer and MQWs region are located at the node and anti-node positions of the electric field, respectively to reduce the absorption from the ITO layer and to further increase the coupling between the electric field and MQWs region. The VCSEL structure was grown on a 2-inch sapphire substrate by the metal-organic chemical vapor deposition (MOCVD) system. The substrate was thermally cleaned in the hydrogen ambient for 5 min at 1100 ℃, and then a 30 nm-thick GaN nucleation layer was grown at 500℃. The growth temperature was raised up to 1100 ℃ for the growth of a 2 μm-thick GaN buffer layer.

The subsequent epitaxial structure consisted of a 29-pair AlN/GaN DBR, a 7λ cavity (λ = 410 nm) including a 860 nm-thick n-GaN layer, 10 pairs InGaN/GaN (2.5 nm/12.5 nm) MQWs, a 24 nm-thick AlGaN layer as the electron blocking layer, a 110 nm-thick p-GaN layer, and a 2 nm-thick p^+ InGaN layer as the contact layer. The AlGaN electron blocking layer was served to reduce the electron overflow to the p-GaN layer. In order to reduce the crack problems encountered in the AlN/GaN DBRs, we inserted one AlN/GaN superlattice into each five DBR periods at first twenty pairs of DBR. Then the superlattice was inserted into each three DBR periods for the remaining nine pairs of DBR to reduce the tensile strain [47]. In the fabrication process, a 200 nm-thick SiN_x layer was deposited by the plasma enhanced chemical vapor deposition as a current confined layer. By this way, the current injection aperture of VCSEL devices was about 10 μm in diameter. Then, a 30 nm-thick ITO layer was deposited as the current spreading layer due to the poor conductivity of the p-GaN layer and annealed at 600 °C for 10 min by rapid thermal annealing. The 2 nm-thick p^+ InGaN layer on the p-GaN surface can further reduce the series resistance between the thin ITO layer and the p-GaN layer with a slight increase of absorption. Then, the p-contact and n-contact were deposited with Ni/Au of about 20 nm/150 nm and Ti/Al/Ni/Au of about 20 nm/150 nm/20 nm/150 nm by the e-gun system, respectively. Finally, 10 pairs Ta_2O_5/SiO_2 of the top dielectric DBR were deposited by the ion-assisted e-gun system to complete the whole GaN-based VCSEL devices. Both of the 29-pair AlN/GaN DBR and the 10-pair Ta_2O_5 DBR show a high reflectivity of over 99 % at the peak wavelength at 410nm in the n-k measurement system. Fig. 4-15(b) shows the charge-coupled device (CCD) image of a VCSEL device injected at 2 mA under CW current injection at room temperature

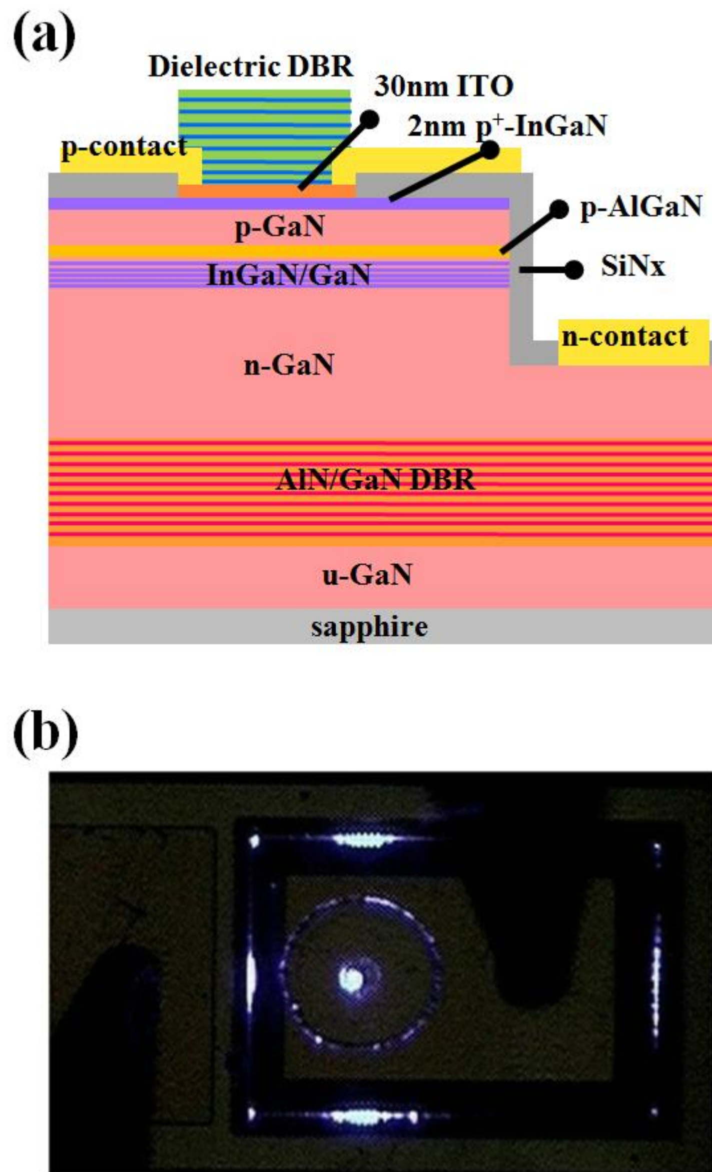

Fig. 4-27(a)VCSEL full structure (b)turn on image at 2mA

The GaN-based VCSEL devices with current injection apertures of about 10 μm in diameter were tested by using a Keithely 238 CW current source. The emission light was collected by a 100 μm diameter multimode fiber and fed into the spectrometer using a grating of 1800 g/mm with a spectral resolution of about 0.15 nm. The output from the spectrometer was detected by a CCD to record the emission

spectrum. The VCSEL devices were then measured at environment temperature at 300 K. Fig. 4-28(a) shows L-I-V curves at 300 K. The dash line is the linear fitting curve of the laser intensity versus injection current. A clear lasing transition from spontaneous emission to stimulated emission can be observed at room temperature. From the linear fitting curve, the laser threshold current is around 9.7 mA corresponding to the current density of about 12.4 kA/cm^2. The relative low threshold at room temperature operation could be due in part to the successful prevention of carrier overflow by using the electron blocking layer on top of the MQWs and the lower internal absorption loss of the thinner ITO layer. The turn-on voltage is about 4.3 V indicating the good electrical contact of the 30 nm ITO transparent layer and the 2 nm-thick InGaN layers. The output laser intensity from the sample increased linearly with current injection beyond the threshold current. However, the laser intensity started to roll over at higher injection current beyond 15 mA due to the thermal effect. We estimated the spontaneous emisson coupling factor from the log-log plot of L-I curve as shown in Fig. 4-28(b). The data points are matched well to the solid fitting line calculated from microcavity laser rate equations [48]. From the curve, we obtained an estmated β value of about 5×10^{-3}.

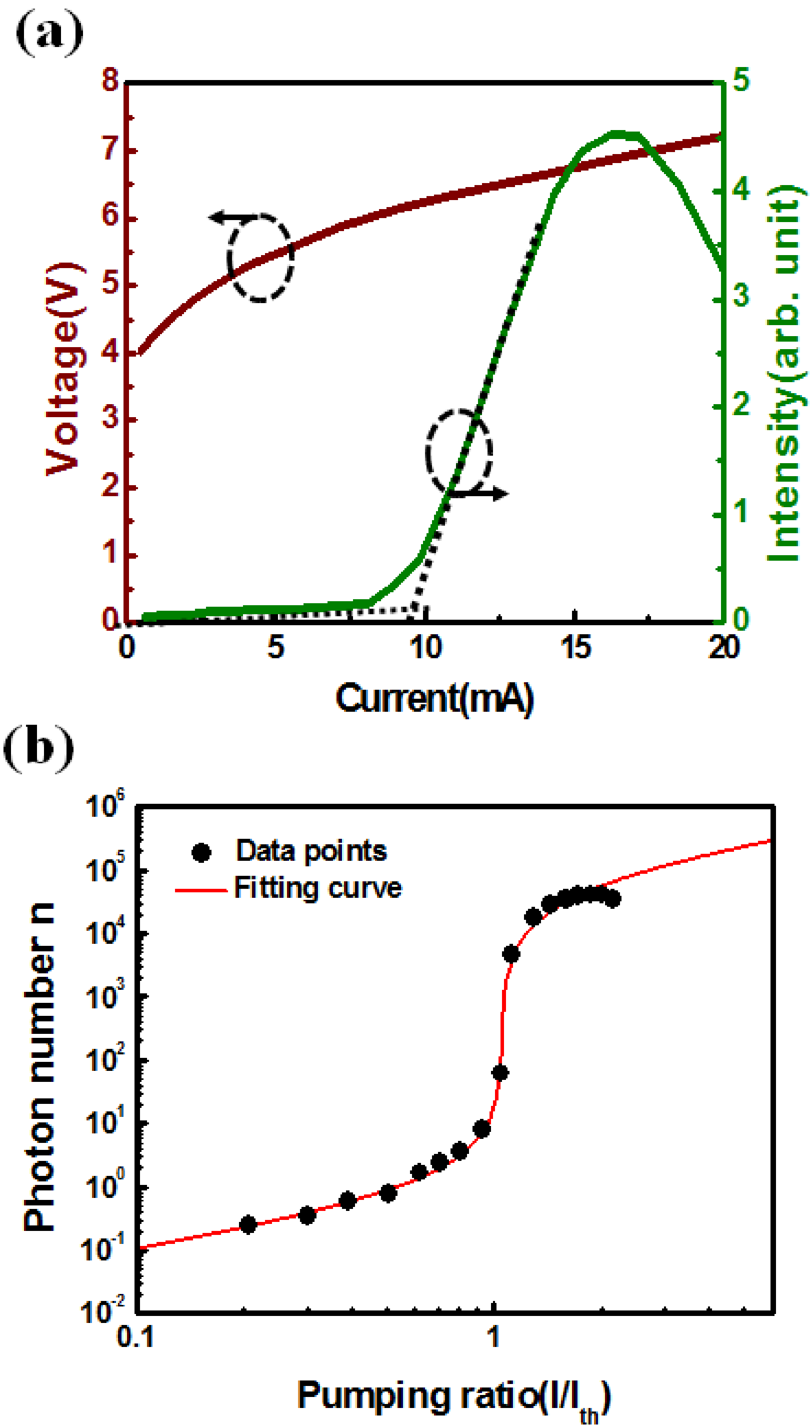

Fig. 4-28(a)LIV curve at 300k (b) coupling factor from the log-log plot of L-I curve

Fig. 4-29(a) shows the emission spectra of our GaN-based VCSEL devices at current injection of 0.6 I_{th}, 1 I_{th} and 1.2 I_{th}, respectively. The laser emission wavelength was measured to be 412 nm with a linewidth of about 0.5 nm. The inset of Fig. 4-29(b) shows the CCD image of a lasing spot size of about 2 μm in diameter. Finally, using the angular-resolved measurement system, the laser intensity at different angles emitted from the GaN-based VCSELs was collected by using a 600 μm fiber. Fig. 4-29(b) shows the measurement data at different angles and the solid curve is the fitting curve. We obtained a laser beam divergence angle of about 8°. Fig. 4-29(c) shows the degree of polarization (DOP) of the laser beam. The solid line is the fitting curve. The DOP value was estimated to be about 55°.

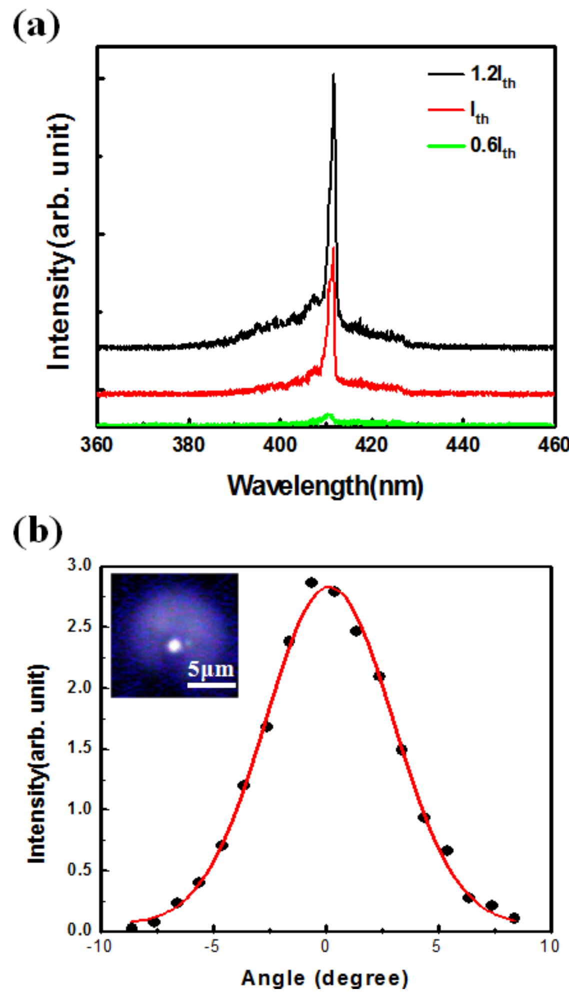

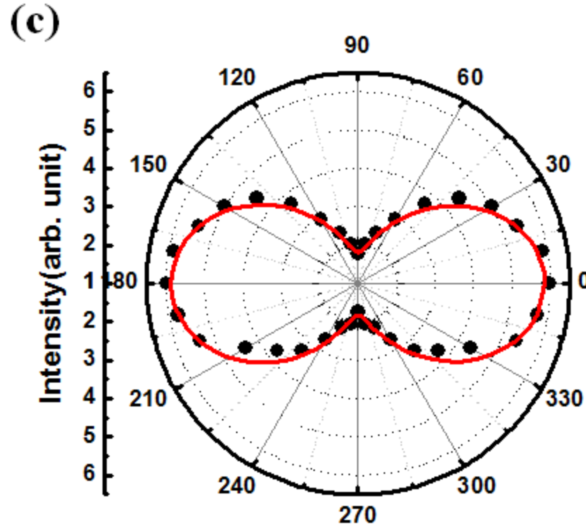

Fig.4-29(a) emission spectra of our GaN-based VCSEL devices at current injection of 0.6 I_{th}, 1 I_{th} and 1.2 I_{th}, respectively (b) the measurement data at different angles and the solid curve is the fitting curve, (insert)the CCD image of a lasing spot size of about 2 μm in diameter.(c) the degree of polarization (DOP) of the laser beam

In summary, we have demonstrated the CW RT operation of GaN-based vertical cavity surface emitting lasers with hybrid mirrors. The laser has a thin Indium-Tin-Oxide layer of 30 nm as the transparent conducting layer combining with a thin heavily doped p-type InGaN contact layer to reduce the optical loss while maintaining good current spreading capability. An AlGaN electric blocking layer on the top of the InGaN multiple quantum well is also inserted to prevent the carrier overflow. At 300K, the laser has a threshold current at 9.7 mA corresponding to 12.4 kA/cm^2. The laser emission wavelength is 412 nm with a linewidth of about 0.5 nm. The laser has an estimated spontaneous emission coupling factor of about 5×10^{-3}. The degree of polarization, and divergence angle of the laser are measured to be 55% and 8°, respectively.

Chapter 5
Characteristics of electrically pumped GaN-based VCSELs with AlN Current Blocking Layer

5.1 Characteristics of AlN[49]

Aluminum nitride is stable at high temperatures in inert atmospheres and melts at 2800 ℃. In a vacuum, AlN decomposes at ~1800 ℃. In the air, surface oxidation occurs above 700℃, and even at room temperature, surface oxide layers of 5-10 nm have been detected. This oxide layer protects the material up to 1370℃. Above this temperature bulk oxidation occurs. Aluminum nitride is stable in hydrogen and carbon dioxide atmospheres up to 980℃.[3]The material dissolves slowly in mineral acids through grain boundary attack, and in strong alkalies through attack on the aluminum nitride grains. The material hydrolyzes slowly in water. Aluminum nitride is resistant to attack from most molten salts, including chlorides and cryolite. Aluminum nitride (AlN) is a nitride of aluminium. Its wurtzite phase (w-AlN) is a wide band gap (6.2 eV) semiconductor material, giving it potential application for deep ultraviolet optoelectronics.

Among the prominent nitride semiconductors such as, GaN, AlN, InN and their alloys, with the notable exception of AlN and its alloys, layers of high-quality most of the materials can be grown at temperatures of 1200 ℃ or less. The crystalline quality of AlN layers is always inferior to its counterpart GaN grown at much lower temperatures. The high temperature growth of AlN films is expected to be effective in

improving crystalline quality and surface morphology because surface migration of Al-species would increase at high temperatures.

Although the high temperature re-growth condition contribute the better quality of AlN film, but it may probably damage the quantum well. As the result, we choose lower temperature conditions to re-growth the AlN current blocking layer.

The re-growth temperatures various from 850°C to 1080°C. We used four probe and AFM to measure the sheet resistance and roughness of AlN. Fig.5.1 shows the AFM of three re-growth conditions, as the temperature rise the morphology of film become more flatness. Table5.1 shows the comparisons of three temperatures in different re-growth condition.

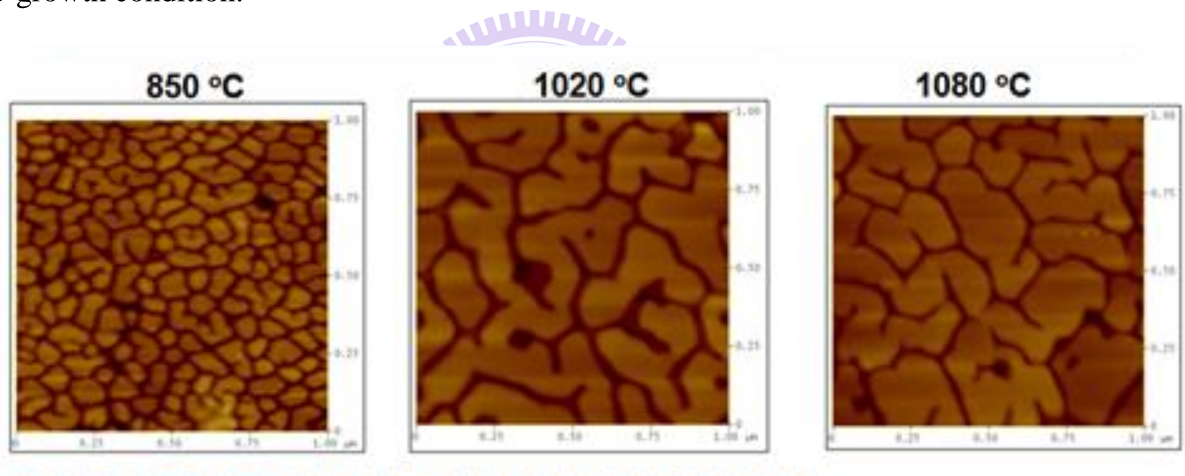

Fig. 5.1 (a) AFM of three AlN re-growth conditions.

	850 °C	1020 °C	1080 °C
Sheet resistance	3~5KΩ	6~8KΩ	6~13KΩ
R.M.S.	3.627nm	2.935nm	2.485nm

Table 5.1 comparison of AlN film

As the result, we choose t he 1020°C as the AlN re-growth condition, due to the sheet resistance and surface roughness is close to 1080°C but higher than 850°C.

After two steps of re-growth we use PL spectrum and NK reflection spectrum to check the quantum well signal .Fig. 5.1(b) shows the after two steps re-growth the quantum well PL spectrum, which still in the center of bottom DBR reflectance. The dip curve in the DBR reflectance indicates the quantum well's absorption through NK measurement.

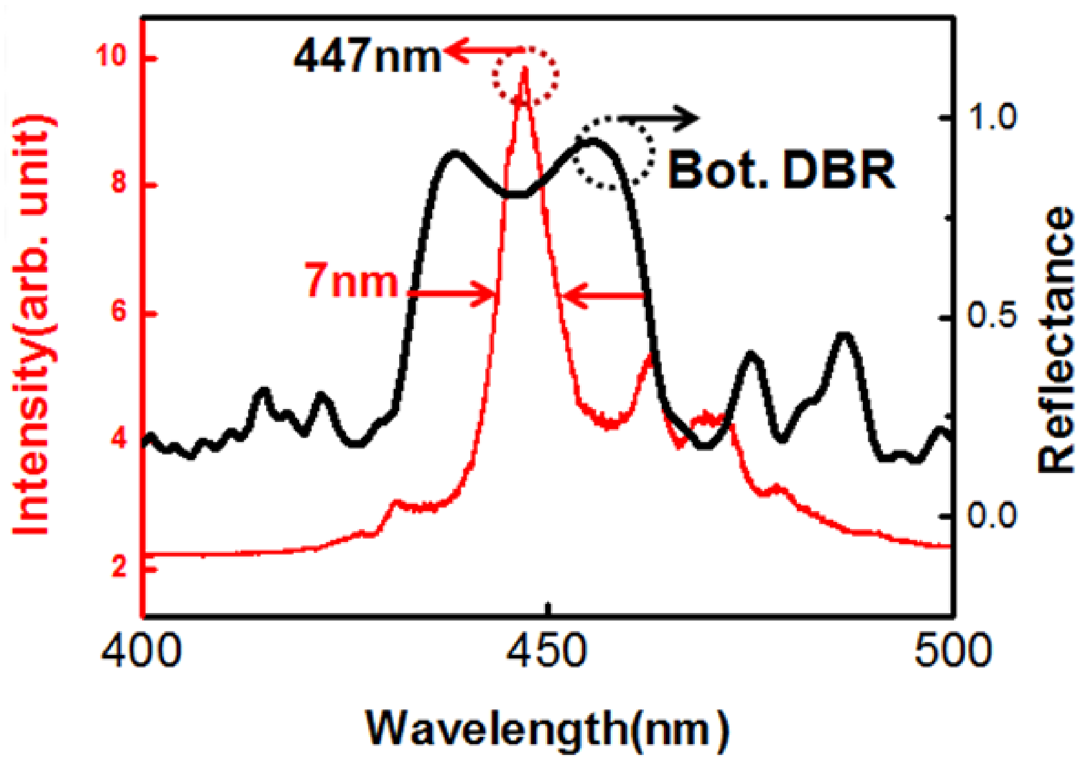

Fig.5.1 (b) PL after two steps re-growth and bottom DBR reflectance.

5.2 Fabrication of GaN-based VCSELs with AlN current blocking layer process

5.2.1 Initial clean and photolithography technique

During process of GaN-based VCSELs, two basic skills will be frequently used. One is the initial clean (I.C.), and another is photolithography technique. The purpose of the I.C. is to remove the small particle, and organism on the sample surface, before we start any process procedure. The steps of I.C. are described as below ：

1. Degreasing by ultrasonic baths in acetone (ACE) 5min.
2. Dipping by ultrasonic baths in isopropyl alcohol (IPA) 5min for organism removed.
3. Rinsing in de-ionized water (D.I. water) 5min for surface clean.
4. Blowing with N_2 gas for surface drying.
5. Baking by hot plate 120°C, 5min, for wafer drying.

The purpose of the photolithography is to transfer the pattern of the mask to the photoresist (PR) on the wafer. In the process of photolithography, a positive photoresist AZ 5214E was used. Although it is positive photoresist , it is capable of image reversal (IR) resulting in the effect of negative photoresist. In fact AZ 5214E is almost exclusively used in the IR-mode which is proper to be used in the lift-off process. Both positive exposure and IR exposure photolithography technique were employed in our VCSEL process. These photolithography techniques are described as below：

Positive exposure technique

1.Spin coating by photoresist (1000rpm/10s, 3500rpm/30s).

2. Soft bake: hot plate 90 ^{o}C, 90sec.

3. Alignment and exposure

4. Development: dipping in AZ-300 for 30sec.

5. check exposure PR pattern by OM.

6. Hard bake: hot plate 120 ^{o}C, 4min

IR exposure technique

1.Spin coating by photoresist (1000rpm/10s, 3500rpm/30s).

2. Soft bake: hot plate 90 ^{o}C, 90sec.

3. Alignment and exposure (about half time of positive exposure)

4.Hard bake 120℃ 110sec

5.Exposure without mask 57sec

6. Development: dipping in AZ-300 for 30sec.

7. check exposure PR pattern by OM.

8. Hard bake: hot plate 120 ^{o}C, 4min

5.2.2 Epitaxial flowchart

The overall GaN VCSEL structure is shown in Fig. 5.1. The mirocavity and bottom DBR structure are grown in a vertical-type MOCVD system (EMCORE D75), which can hold one 2-inch sapphire wafer. The nitride-based DBR used in the experiment is the stacks of 29-pair AlN/GaN layers with insertion of the AlN/GaN super-lattice (SL). The super-lattice in structure is inserted for releasing strain during the growth of AlN/GaN DBR to further improve interface and raise reflectivity of the DBR. Fig. 5.2 is the reflectance spectrum of bottom DBR, and there is a high reflectivity (~97%) at

447nm. The stop band of bottom DBR is as wide as about 20nm.

Then, a micro-cavity formed by a p-n junction was grown following the growth of the DBR structure. The micro-cavity composed of about 900-nm-thick n-type GaN, a ten pairs $In_{0.2}Ga_{0.8}N$/GaN (2.5 nm/10.5 nm) MQW, 24nm AlGaN electron blocking layer , 20nm p-GaN, 30nm AlN current blocking layer and 155nm p-GaN as shown in Fig. 5.3.

The AlN VCSEL epitaxial flowchart was fabricated by five steps. In the beginning, SiO2 hard mask was used to define current aperture. The SiO2 was grown by PECVD patterned to define the current confinement layer with the effective current aperture varying from 3µm to 10µm, as shown in Fig. 5.4.

The 30nm AlN layer process is epitaxial by a vertical-type MOCVD system (EMCORE D75) and the epitaxial environment at 1020°C and 100 torr. After liftoff SiO2 by using BOE(as shown in Fig.5.5), the surface is clear . In this step, we must check the surface is clear and without SiO2, the remain SiO2 will to impede the p-GaN re-growth. Lastly the p type GaN 130nm and 2nm InGaN layer were re-growth. The 2nm InGaN layer is used for reduction the Schottky barrier height between ITO and p-GaN layer, and it can also improve current spreading when current injection. The PL spectrum and reflectance spectrum of VCSEL sample without upper DBR are shown in Fig.5.1 (b) previous chapter. The dominate wavelength and FWHM are 447 and 7nm respectively.

Fig.5.1.1 The overall diagram of VCSEL structure

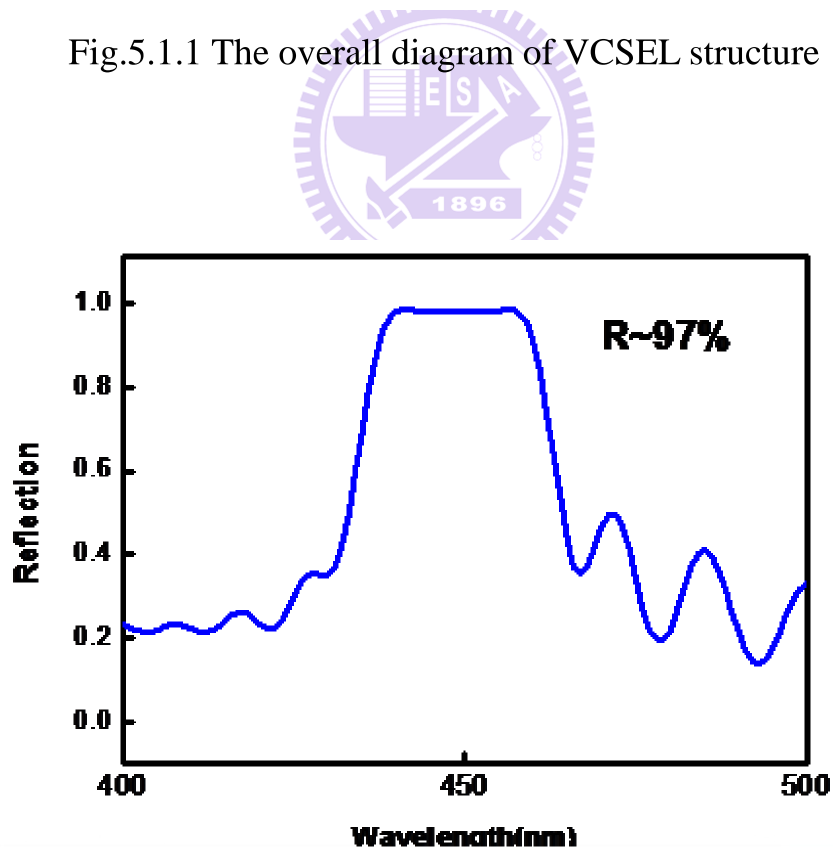

Fig. 5.2 The reflection spectrum of bottom DBR

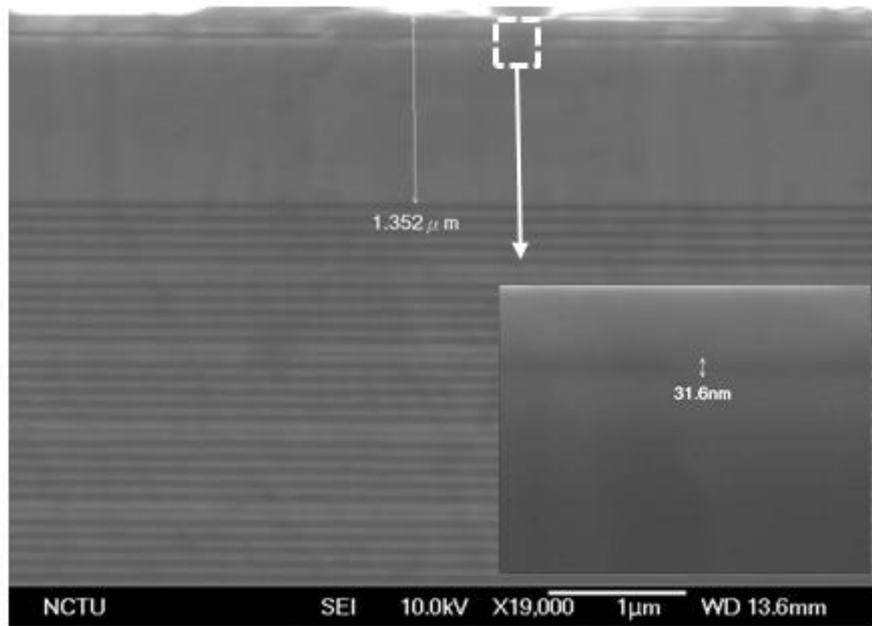

Fig.5.3 The cross section SEM image of VCSEL cavity without upper DBR, the insert figure is the thickness of AlN layer.

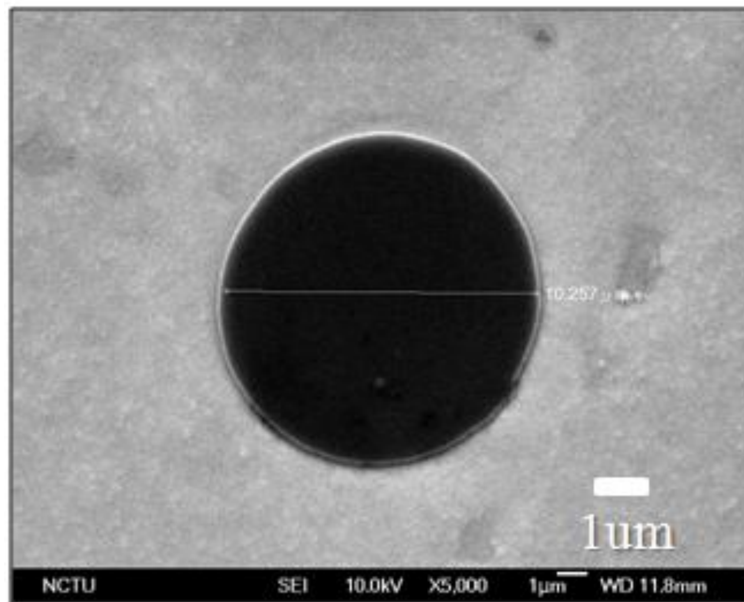

10um

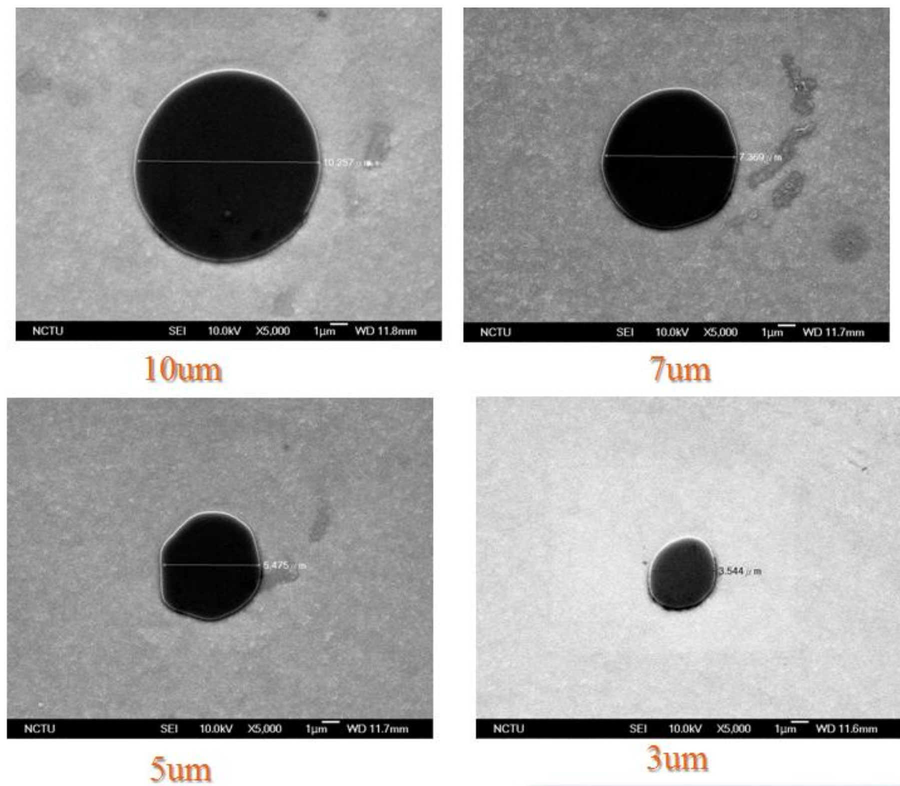

Fig. 5.4 current aperture defined by SiO2.varying from 3um to 10um

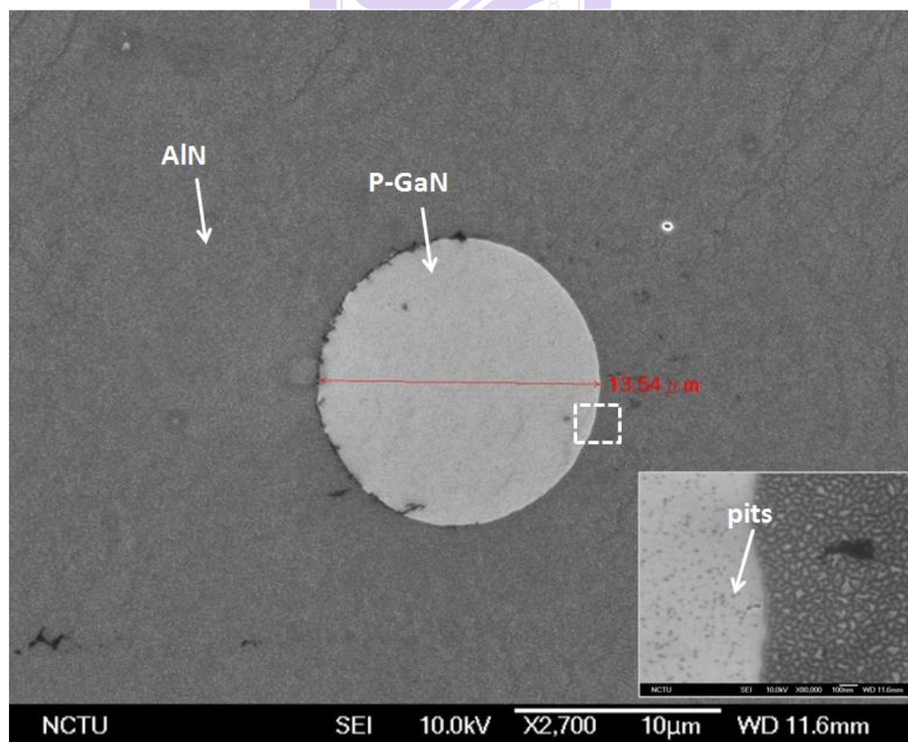

Fig. 5.5 The p-GaN surface after liftoff SiO2 and the insert figure point out the pits on p-GaN

5.2.3 Process flowchart

The AlN- VCSEL was fabricated by six process steps. In the beginning, mesa was etched by ICP dry etching, as shown in Fig. 5.7. Then 200nm SiNx layer was deposited by PECVD and patterned to defined current injection aperture as shown in Fig. 5.8. The 30nm ITO were deposited by sputter and annealed at oven 2hr and nitrogen ambient. The inner diameter is 25um and the outer diameter is 80um as shown in Fug. 5.9 .Through the ring shape ITO the VCSEL cavity will become an ideally cavity without ITO absorption. At current injection, the current will laterally spreading into aperture (mark in Fig.5.9.2) by high sheet resistance of AlN current blocking layer and the turn on image is shown in Fig. 5.9.1. The Ti/Al/Ni/Au and Ni/Au contacts were deposited to serve as n-type and p-type electrode respectively, as shown in Fig. 5.10. The VCSEL was completed by capping the structure with 10 periods of SiO2/Ta2O5 DBR stack (R~99%), as shown in Fig. 5.11

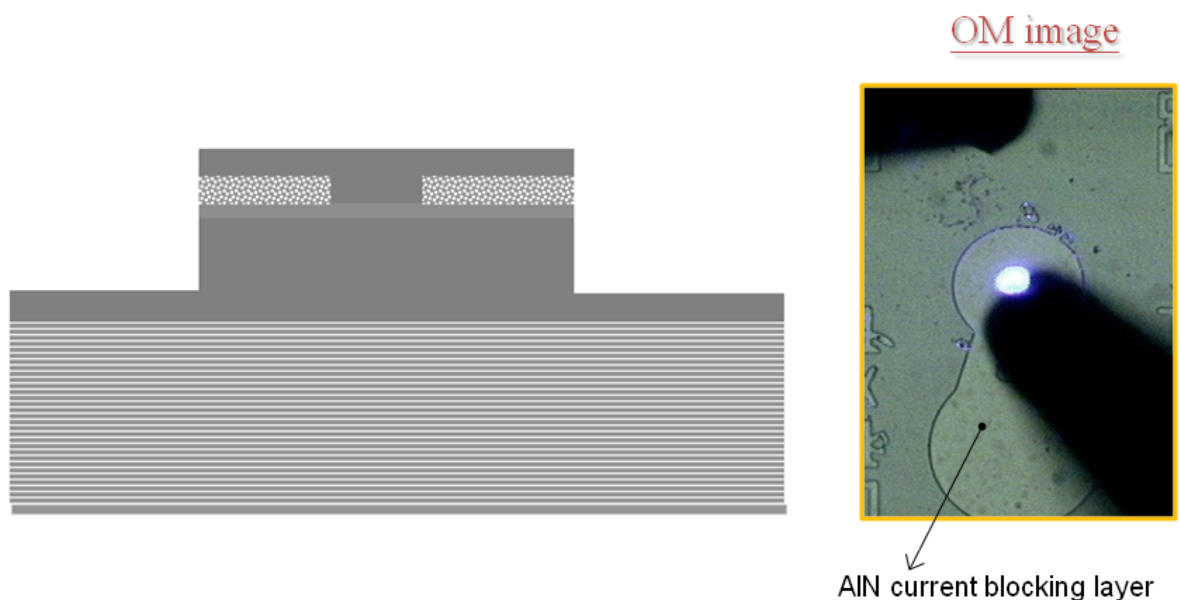

Fig. 5.7 Mesa etching step and the device turn on image

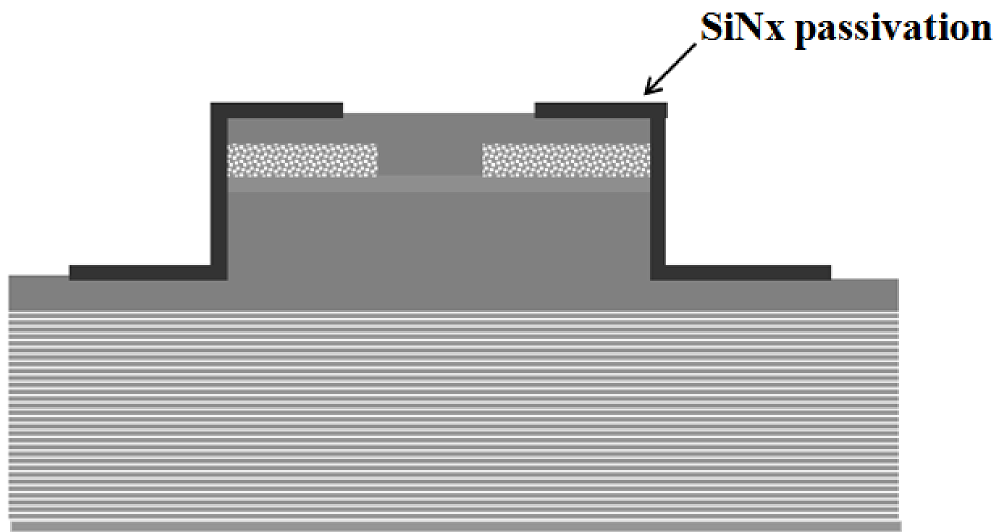

Fig. 5.8 Deposited SiNx as the passivation layer

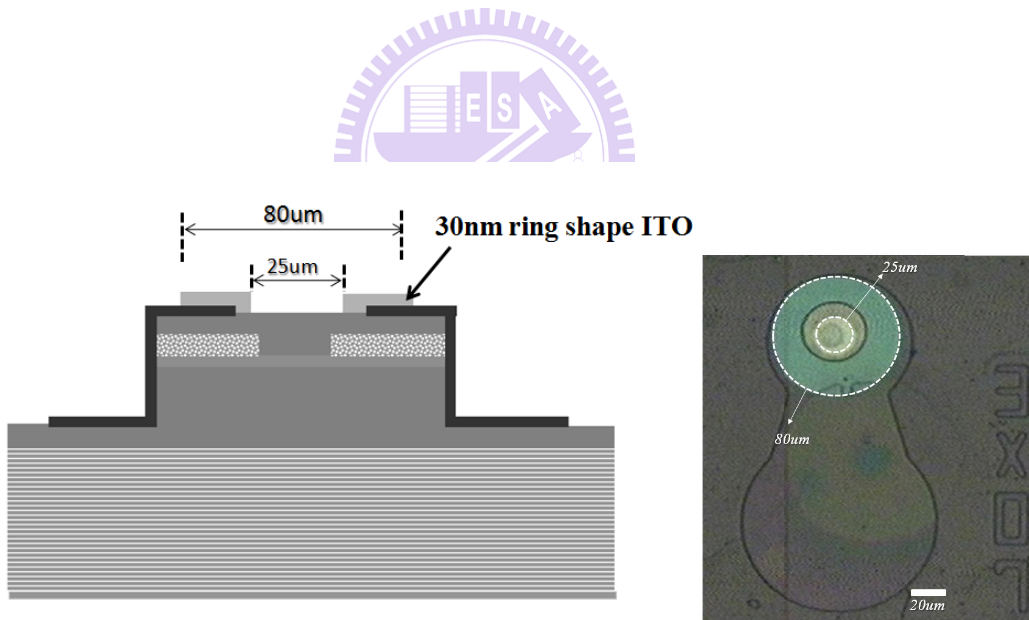

Fig.5.9.1 The ring shape ITO

Fig. 5.9.2 The ring shape ITO and its CCD image.

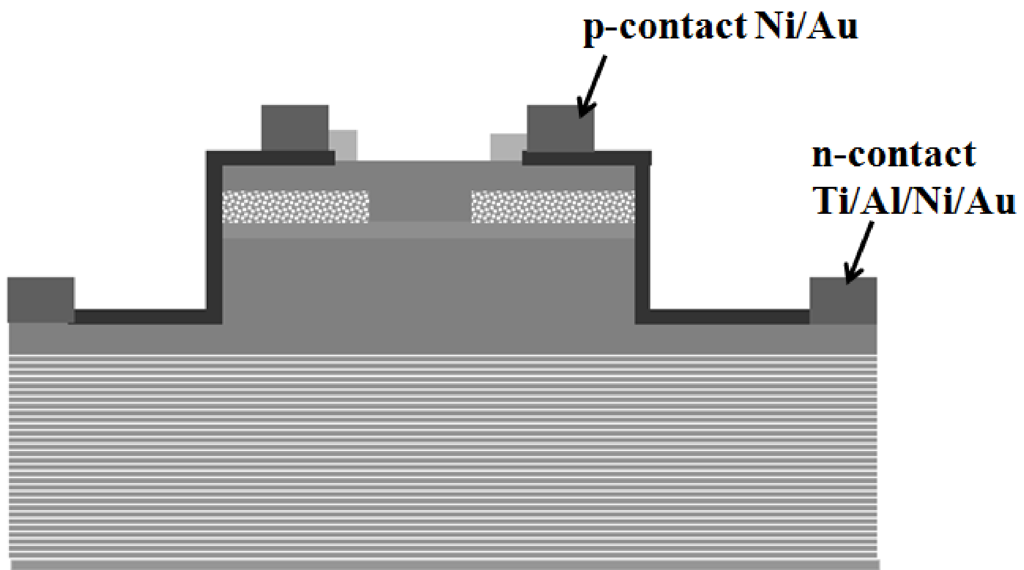

Fig. 5.10 deposited n-contact and p-contact

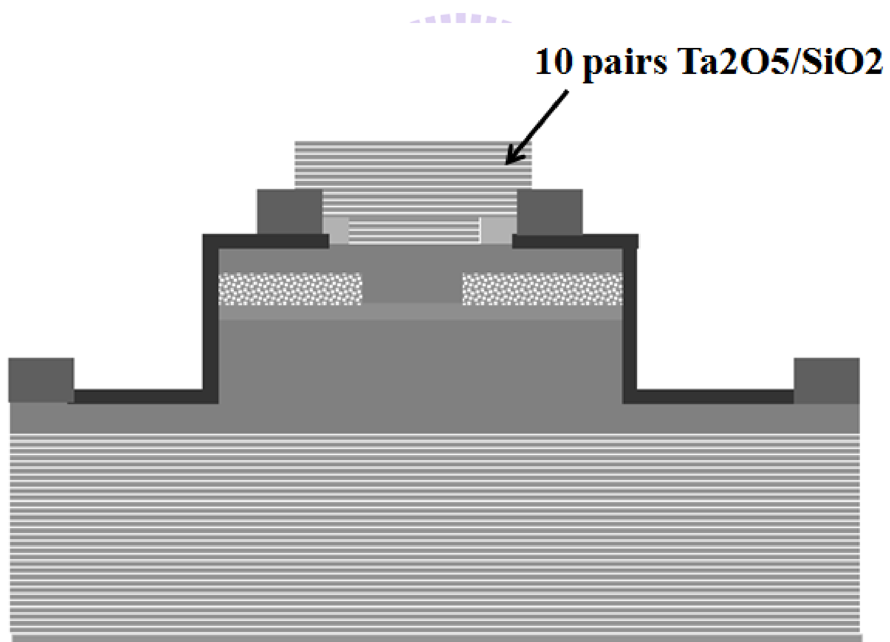

Fig. 5.11 Deposited 10-pair Ta_2O_5/SiO_2 DBR

5.3Characteristics of electrically pumped GaN-based VCSELs with AlN current blocking layer(CBL)

5.3.1 The emission images of AlN VCSEL

Figure 5.12 shows the light emission photograph of AlN-VCSEL operated at 0.03mA. The bright apertures show AlN layer can effective block the current. The sizes of aperture were defined 3um, 5um, 7um, 10um.. We can clearly find the light emission is concentrate in the current aperture defined by AlN.

In order to observe more detail in the current aperture, we also observed the optical intensity distribution by means of CCD and Beam-view program. The color on Fig 5.12(c) represents the relative optical intensity emitted from observed device, and this figure shows the current injection uniformly into the aperture. We can observe the light beam showing a Guass distribution in Fig. 5.12(d).Fig. 5.8 shows the VCSEL before contact process image, the ring shape ITO with 25um and 80 um, inner and outer diameter respectively. Fig. 5.9 shows the turn on image of VCSEL without ITO layer, which injection current laterally flow through p-GaN layer. The concentrated emission light not only confirms that current is uniformity injection into the current aperture but also shows that the AlN plays a role of current blocking layer successfully.

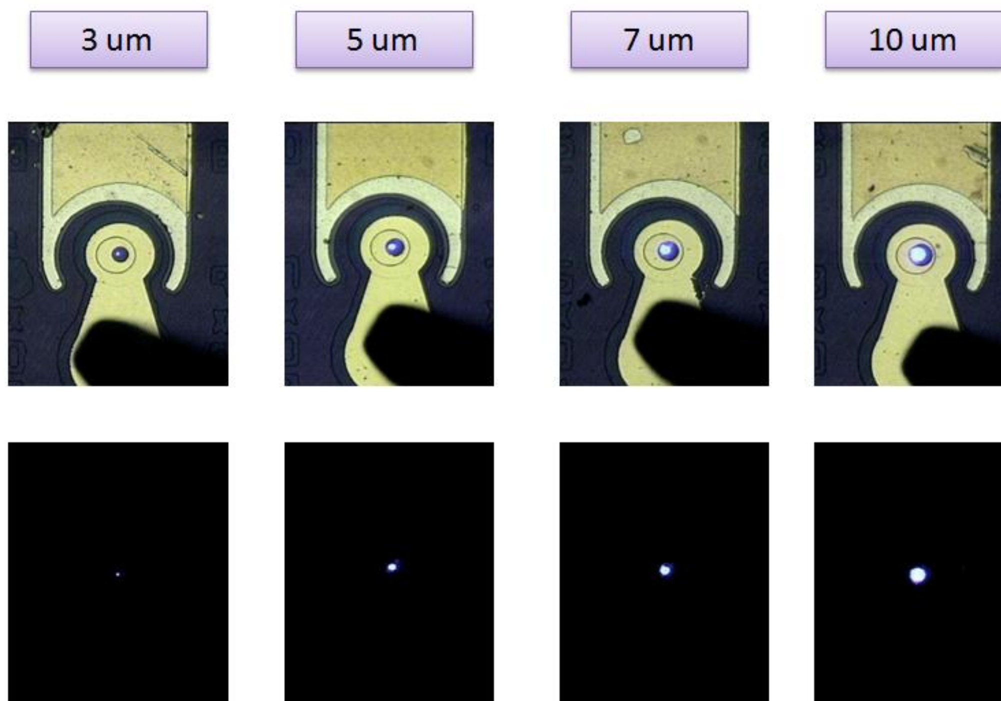

Fig. 5.12 Emission images of AlN VCSEL

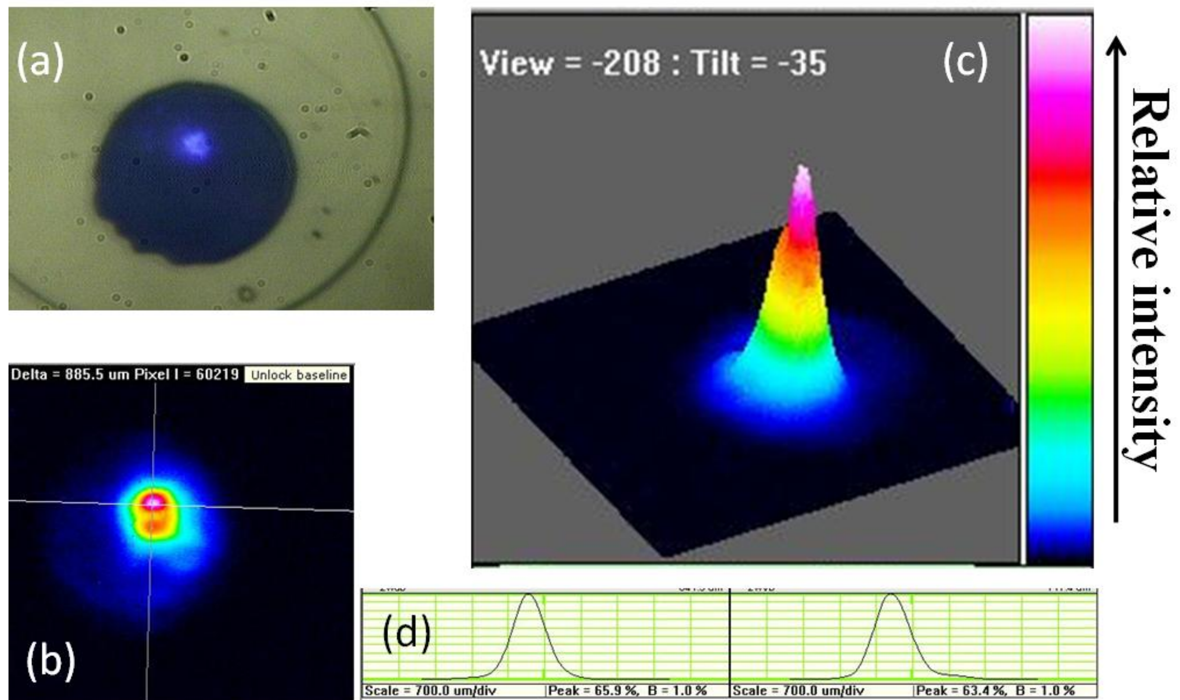

Fig. 5.13 (a) The emission image of aperture size of 3μm under high magnification CCD image (b)(c)(d)Beam-view on 3um aperture emission

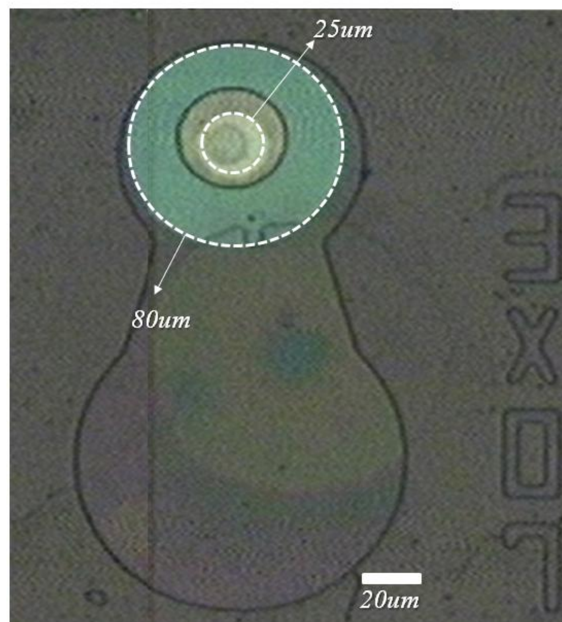

Fig. 5.8 The ring shape ITO and CCD image.

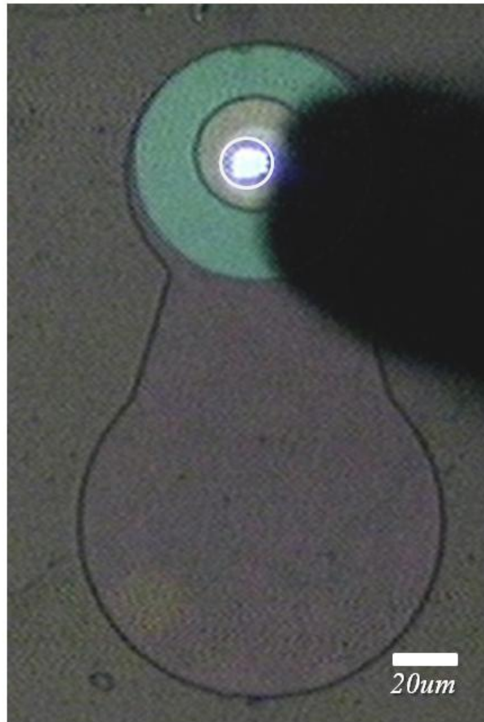

Fig. 5.9 Current lateral spreading by AlN current blocking, the white mark point out the 10um current aperture.

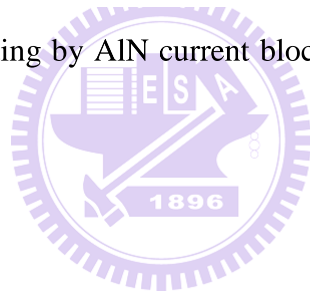

5.3.2The L- I-V curves of AlN blocking layer and conventional VCSEL

The current-voltage (I-V) characteristics of AlN and conventional device are both shown in Figure 5.14. The turn on voltage and resistance of the conventional VCSEL which is 10um current aperture define by SiNx passivation was about 7.14V and 385Ω respectively. The 10um current aperture of VCSEL with AlN CBL shows 7.3V and 389Ω respectively. The slightly higher voltage and resistance compared with the conventional device because the current path could be longer than the conventional VCSEL, such results are realizable and acceptable.

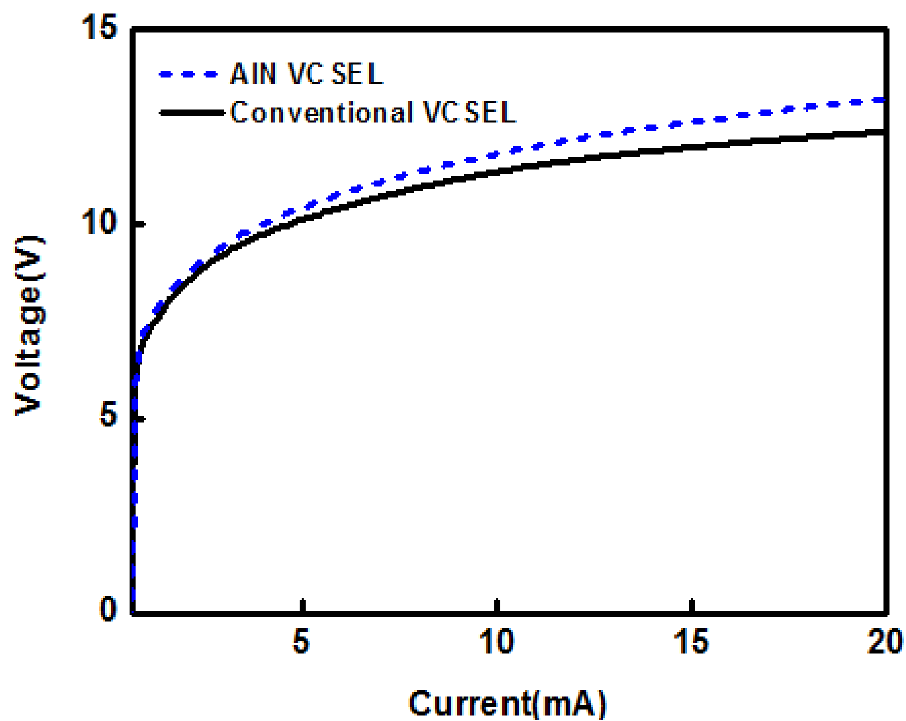

Fig.5.14 I-V curve

5.3.3The optical characteristics of AlN VCSEL

Fig.5.16 shows the AlN VCSEL device structure and turn on image. Fig. 5.17(a) shows the EL spectrum of AlN VCSEL. The equation, which associates the quality factor and total loss, is as follow:

$$Q = \frac{\lambda}{\Delta\lambda} = \frac{2\pi nL}{\lambda\delta}$$

By the equation, the quality factor estimated about 1100, which is at the same order we have measured with the bottom DBR reflection 99.5%.

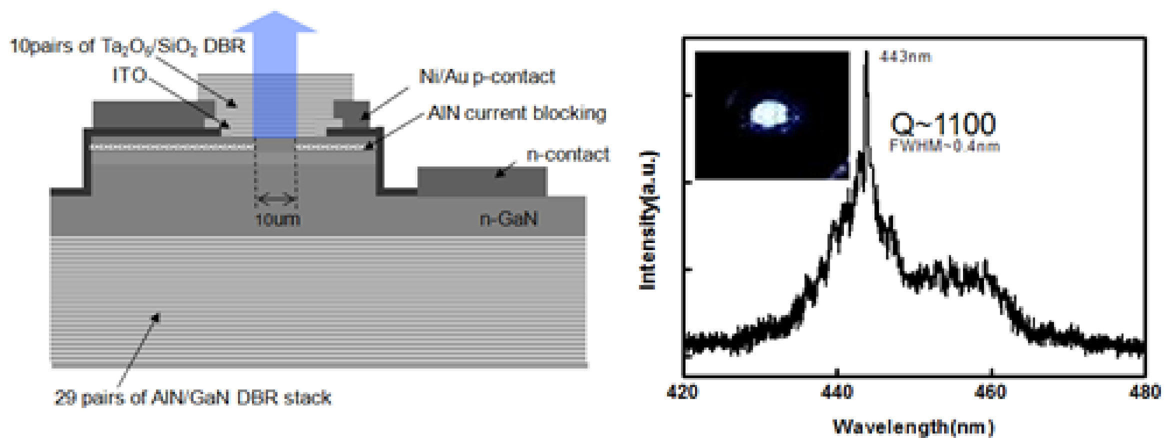

Fig.5.15AlN VCSEL structure and CCD image of 10um aperture.

The EL spectrum and divice structure of AlN and conventional device are both shown in Figure 5.17. In the EL spectrum, take ring shape ITO layer as contact layer shows a high Q (1100) than circular ITO shape (650). This information would cause by the cavity without ITO layer become a more ideally resonant cavity, which is effective reduce the optical loss.

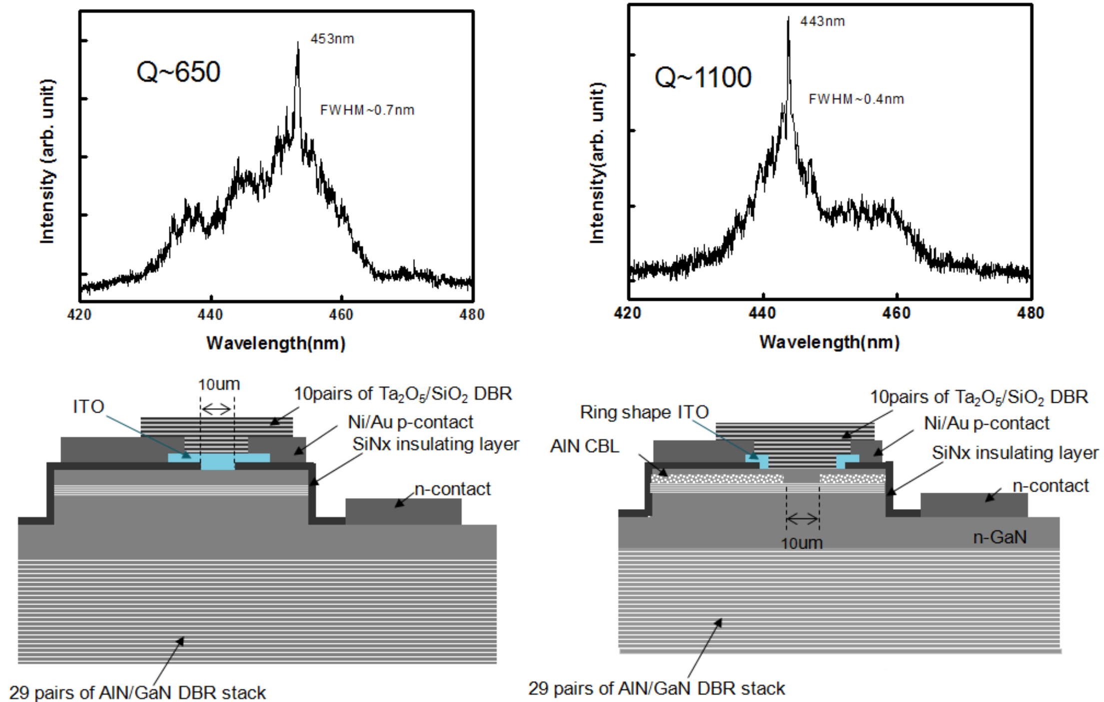

Fig. 5.16EL spectrum and structure of conventional and AlN CBL device.

5.4 Summary

In summary, GaN-based vertical cavity surface emitting laser using AlN re-growth on MQWs for current blocking layer is fabricated and measured. The re-growth temperature and pressure are 1020°C and 100torr respectively. At the same DBR reflectance, the cavity without ITO layer shows a high Q (1100) than conventional device (650). The turn on voltage and series resistance were 7.3V and 389Ω respectively, which close the conventional device with the same current aperture. The current blocking layer not only confines the injection current but also can makes cavity become a more ideally resonant cavity by taking away the ITO layer. These characteristic suggests that AlN current blocking layer during the process of GaN-based VCSEL should be an effective and feasible way for current confinement and reduce the optical loss.

Chapter 6
Conclusions

In conclusion, a 7λ GaN-based VCSEL using AlN as current blocking layer was fabricated and measured. The AlN layer re-growth condition is 1020oC and 100torr is determined. The AlN layer R.M.S and sheet resistance are 2.93nm and 8KΩ respectively. The device structure is composed of high-reflectivity AlN/GaN bottom DBRs (97%) and SiO2/Ta2O5 top DBRs (99%). The turns on voltage and series resistance were about 7.35V and 389Ω respectively. The emission peak wavelength of the AlN VCSEL was located at 447nm with a narrow line-width of 0.4nm. Compared to the emission spectrum of the bottom DBR reflection 99.5% device, the device with bottom DBR reflection 97% shows the same order Q factor of 1100, which without ITO layer. Moreover, the degrees of polarization of about 88.7% were measured. The high degrees of polarization might elucidate optical confined in the VCSEL cavity. While the reason for high degrees of polarization might attribute to the low refractive index of AlN .However, we have not measured the threshold current, which may be attributed to lack of reflection from bottom DBR. But the improvement of Q factor proves that taking AlN as current blocking layer indeed plays an important role to fabricate this kind of high Q device like VCSEL. In order to achieve a certain both upper and bottom DBR reflectivity in requirements and solve the heat dissipation problem due to worse thermal conductivity of sapphire substrate, we may also choose laser liftoff process in our VCSEL structure. We expect combine the AlN structure and laser liftoff technique and finally reach the optimum structure in GaN-based VCSEL.

References

[1] S. Nakamura, M. Senoh, N. Iwasa, and S. Nagahama, *Jpn. J. Appl.Phys.*, **34**, L797 (1995)

[2] S. Nakamura, T. Mukai, and M. Senoh, *Appl. Phys. Lett.*,**64**, 1687 (1994)

[3]S. Nakamura, M. Senoh, S.Nagahama, N.Iwasa, T. Yamada, T. Matsushita, Y. Sugimoto,and H.Kiyoku, *Appl. Phys. Lett.*, **70**, 868 (1997)

[4] S. Nakamura, *Science*, **281**, 956 (1998)

[5] Y. Arakawa, *IEEE J. Select. Topics Quantum Electron.*, **8**, 823 (2002)

[6] H. Morkoc, *Nitride Semiconductors and Devices (Spring Verlag, Heidelberg)* (1999)

[7] S. N. Mohammad, and H. Morkoc, *Progress in Quantum Electron.*, **20**, 361 (1996)

[8] J. I. Pankove, E. A. Miller, J. E. Berkeyheier, *J. Luminescence*, **5**, 84 (1972)

[9] H. P. Maraska, D. A. Stevenson, J. I. Pankove, *Appl. Phys. Lett.*, **22**, 303 (1973)

[10] J. I. Pankove, *Phys. Rev. Lett.*, **34**, 809 (1975).

[11]M. Takeya, T. Tojyo, T. Asano, S. Ikeda, T. Mizuno, O. Matsumoto, S. Goto, Y. Yabuki, S. Uchida, and M. Ikeda, *phys. stat. sol. (a)*, **192**, 269 (2002)

[12] S. Nakamura, M. Senoh, S. Nagahama, N. Iwasa, T.Yamada, T. Matsushita, H. Kiyoku, Y. Sugimoto, T. Kozaki, H. Umemoto, M. Sano, and K. Chocho, *Appl. Phys. Lett.*, **72,** 211 (1998)

[13] S. Nakamura, *IEEE J. Select. Topics Quantum Electron.*, **4**, 483 (1998)

[14] M. C. Schmidt, K. C. Kim, R, M. Farrell, D. F. Feezell, D. A. Cohen, M. Saito, K. Fujito, J. S. Speck, S. P. Denbaars, and S. Nakamura, *Jpn. J. Appl. Phys*, **46**, L190 (2007)

[15] D. F. Feezell, M. C. Schmidt, Robert M. Farrell, K. C. Kim, M. Saito, K. Fujito, D. A.Cohen, J. S. Speck, S. P. Denbaars, and S. Nakamura, *Jpn. J. Appl. Phys*, **46**,

L284 (2007)

[16] K. Iga, *IEEE J. Quantum Electron.*, **24**, 1845 (1988)

[17] K.Iga, *Proceedings of the First International Symposium on blue lasers and light emitting diodes*, Th-11 (1996)

[18] T. Someya, R.Werner, A. Forchel, M. Catalano, R. Cingolani, Y.Arakawa, Science, **285**,1905 (1999)

[19] Y.-K. Song, H. Zhou, M. Diagne, A. V. Nurmikko, R. P. Schneider, Jr., C. P. Kuo, M. R. Krames, R. S. Kern, C. Carter-Coman, and F. A. Kish, *Appl. Phys. Lett.*, **76**, 1662 (2000)

[20] T. Tawara, H. Gotoh, T. Akasaka, N. Kobayashi, and T. Saitoh, *Appl. Phys. Lett.*, **83**, 830 (2003)

[21] H. Zhou, M. Diagne, E. Makarona, A. V. Nurmikko, J. Han, K. E. Waldrip and J. J. Figiel, *Electron. Lett.*, **36**,1777 (2000)

[22] J.T. Chu *et. al.*, *Jpn. J. Appl. Phys*, **45**, 2556 (2006).

[23] Yu Higuchi, Kunimichi Omae , Hiroaki Matsumura, and Takashi Mukai *Applied Physics Express* **1** , 121102 (2008)

[24] J. T. Chu *et. al.*, *Appl. Phys. Lett.*, **89**, 121112 (2006).

[25]. C. C. Kao *et. al.*, *Appl. Phys. Lett.*, **87**, 081105-1 (2005).

[26] C. C. Kao *et. al.*, *IEEE Photon. Technol. lett.*, **18**, 877 (2006).

[27] J. F. Carlin, J. Dorsaz, E. Feltin, R. Butté, N. Grandjean, M. Ilegems, and M. Laügt, *Appl.Phys. Lett.*, **86**, 031107 (2005)

[28] E. Feltin, R. Butté, J. F. Carlin, J. Dorsaz, N. Grandjean, and M. Ilegems, *Electron. Lett.*,**41**, 94 (2005)

[29] T. Ive, O. Brandt, H. Kostial, T. Hesjedal, M. Ramsteiner, and K. H. Ploog, *Appl. Phys. Lett.*, **85**, 1970 (2004)

[30] H.H. Yao, C.F. Lin, H.C. Kuo, S.C. Wang, *J. Crystal Growth,* **262***,* 151 (2004)

[31] S. Kako, T. Someya, and Y. Arakawa, *Appl. Phys. Lett.*, **80**, 722 (2002)

[32] T. Honda, H. Kawanishi, T. Sakaguchi, F. Koyama and K. Iga, *MRS Internet J. Nitride Semicond.* **4S1**, G6.2-1 (1999).

[33] H. E. Li and K. Iga, Vertical-Cavity Surface –Emitting Laser Devices, Springer-Verlag, Berlin, (2003)

[34] C. W. Wilmsen, H. Temkin, L. A. Coldren, Vertical-Cavity Surface-Emitting Lasers, Cambridge University Press (1999)

[35] D. I. Babic and S. W. Corzine, IEEE J. Quantum Electron., 28, 514 (1992)

[36] H. Benisty, H. D. Neve, and C. Weisbuch, IEEE J. Quantum Electron., 34, 1612 (1998)

[37] H. Benisty, H. D. Neve, and C. Weisbuch, IEEE J. Quantum Electron., 34, 1632 (1998)

[38] S. Nakamura, M. Senoh, S. Nagahama, N. Iwasa, T. Yamada, T. Matsushita, Y.Sugimoto, and H. Kiyoku, Appl. Phys. Lett., 70, 868 (1997)

[39] S. Nakamura, Science, 281, 956, (1998)

[40] Y.-K. Song, H. Zhou, M. Diagne, I. Ozden, A Vertikov, A. V. Nurmikko C. Carter-Coman, R. S. Kern, F. A. Kish, and M. R. Krames, Appl. Phys. Lett., 74, 3441, (1999)

[41] T. Someya, K. Tachibana, J. Lee, T. Kamiya and Y.Arakawa, Jpn. J. Appl. Phys., 37, L1424, (1998)

[42] T. C. Lu, C. C. Kao, H. C. Kuo, G. S. Huang, and S. C. Wang, Appl. Phys. Lett., 92, 141102 (2008)

[43] Y. Higuchi, K. Omae, H. Matsumura, and T. Mukai, Appl. Phys. Exp., 1, 121102 (2008)

[44] K. Omae, Y. Higuchi, K. Nakagawa, H. Matsumura, and T. Mukai, Appl. Phys. Exp., 2, 052101 (2009)

[45] S. C. Wang, T. C. Lu, C. C. Kao, J. T. Chu, G. S. Huang, H. C. Kuo, S. W. Chen, T. T. Kao, J. R. Chen, and L. F. Lin, Jpn. J. Appl. Phys., V46, No. 8B, 5397-5407, (2007)

[46] J. R. Chen, C. H. Lee, T. S. Ko, Y. A. Chang, T. C. Lu, H. C. Kuo, Y. K. Kuo, and S. C. Wang, IEEE J. Lightwave Tech., 26 No.3, 329 (2008)

[47] G. S. Huang, T. C. Lu, H. H. Yao, H. C. Kuo, S. C. Wang, C. W. Lin, and L. Chang, Appl. Phys. Lett., 88, 061904 (2006)

[48] G. Bjork and Y. Yamamoto, IEEE J. Quantum. Electron., 27, 2386(1991)

[49] L. I. Berger (1997). Semiconductor materials. CRC Press. pp. 123–124.